

Accepted Manuscript

Formation of abiotic hydrocarbon from reduction of carbonate in subduction zones: Constraints from petrological observation and experimental simulation

Renbiao Tao, Lifei Zhang, Meng Tian, Jianjiang Zhu, Xi Liu, Jinzhong Liu, Heidi E. Höfer, Vincenzo Stagno, Yingwei Fei

PII: S0016-7037(18)30436-8
DOI: <https://doi.org/10.1016/j.gca.2018.08.008>
Reference: GCA 10881

To appear in: *Geochimica et Cosmochimica Acta*

Received Date: 11 December 2017
Revised Date: 18 July 2018
Accepted Date: 3 August 2018

Please cite this article as: Tao, R., Zhang, L., Tian, M., Zhu, J., Liu, X., Liu, J., Höfer, H.E., Stagno, V., Fei, Y., Formation of abiotic hydrocarbon from reduction of carbonate in subduction zones: Constraints from petrological observation and experimental simulation, *Geochimica et Cosmochimica Acta* (2018), doi: <https://doi.org/10.1016/j.gca.2018.08.008>

This is a PDF file of an unedited manuscript that has been accepted for publication. As a service to our customers we are providing this early version of the manuscript. The manuscript will undergo copyediting, typesetting, and review of the resulting proof before it is published in its final form. Please note that during the production process errors may be discovered which could affect the content, and all legal disclaimers that apply to the journal pertain.



Revision 2

Formation of abiotic hydrocarbon from reduction of carbonate in subduction zones: Constraints from petrological observation and experimental simulation

Renbiao Tao^a, Lifei Zhang^{a*}, Meng Tian^a, Jianjiang Zhu^a, Xi Liu^a, Jinzhong Liu^b, Heidi E. Höfer^c, Vincenzo Stagno^d, Yingwei Fei^{a,e}

^aThe MOE Key Laboratory of Orogenic Belt and Crustal Evolution, School of Earth and Space Sciences, Peking University, Beijing 100871, China

^bState Key Laboratory of Organic Geochemistry, Guangzhou Institute of Geochemistry, Chinese Academy of Sciences, Guangzhou 510640, China

^cInstitut für Geowissenschaften, Mineralogie, Goethe-Universität, 60438 Frankfurt am Main, Germany.

^dDepartment of Earth Sciences, Sapienza University of Rome, Rome, 00185, Italy.

^eGeophysical Laboratory, Carnegie Institution of Washington, Washington, DC 20015, USA

*Corresponding author.

E-mail address: Lfzhang@pku.edu.cn.

Abstract

Subduction is a key process for linking the carbon cycle between the Earth's surface and its interior. Knowing the carbonation and decarbonation processes in the subduction zone is essential for understanding the global deep carbon cycle. In particular, the potential role of hydrocarbon fluids in subduction zones is not well understood and has long been debated. Here we report graphite and light hydrocarbon-bearing inclusions in the carbonated eclogite from the Southwest (S.W.) Tianshan subduction zone, which is estimated to have originated at a depth of at least 80 kilometers. The formation of graphite and light hydrocarbon likely results from the reduction of carbonate under low oxygen fugacity (~ FMQ - 2.5 log units). To better understand the origin of light hydrocarbons, we also investigated the reaction between iron-bearing carbonate and water under conditions relevant to subduction zone environments using large-volume high-pressure apparatus. Our high-pressure experiments provide additional constraints

on the formation of abiotic hydrocarbons and graphite/diamond from carbonate-water reduction. In the experimental products, the speciation and concentration of the light hydrocarbons including methane (CH_4), ethane (C_2H_6), and propane (C_3H_8) were unambiguously determined using gas chromatograph techniques. The formation of these hydrocarbons is accompanied by the formation of graphite and oxidized iron in the form of magnetite (Fe_3O_4). We observed the identical mineral assemblage (iron-bearing dolomite, magnetite, and graphite) associated with the formation of the hydrocarbons in both naturally carbonated eclogite and the experimental run products, pointing toward the same formation mechanism. The reduction of the carbonates under low oxygen fugacity is, thus, an important mechanism in forming abiotic hydrocarbons and graphite/diamond in the subduction zone settings.

1. Introduction

Subduction is considered as a factory for the recycling of elements such as carbon between the Earth's interior and surface (Hacker, 2003; Tatsumi, 2005). It plays a key role in the deep carbon cycle (Javoy *et al.*, 1982; Dasgupta, 2013). Carbon is recycled into the Earth's interior via subduction of different carbon-bearing phases (e.g., carbonate), and it is partly released to the surface by metamorphism in the subduction zone and volcanism at islands arcs (Berner, 1999; Sleep and Zahnle, 2001). Therefore, knowing the behavior of the carbon-bearing phases in the subduction zone is of particular interest for understanding the global deep carbon cycle (Ague and Nicolescu, 2014; Kelemen and Manning, 2015; Poli, 2015; Megan and Dasgupta, 2017).

Most of the previous studies on the stability of the carbon-bearing phases at the subduction condition focused on the variables of pressure and temperature (Isshiki *et al.*, 2004; Poli *et al.*, 2009). In fact, the redox conditions also control the speciation and stability of carbon-bearing

phases during subduction, which is still poorly explored (Connolly, 1995; Galvez *et al.*, 2013). Taken a carbon-saturated C-O-H fluid as an example, the ratio of CH₄ and CO₂ varies with redox condition of the system (Connolly, 1995). Therefore, defining the oxygen fugacity (f_{O_2}) of the subducting slab is necessary in order to discuss the stability of different carbon forms (e.g. graphite and hydrocarbons). In the subduction zone, the speciation, mobility, and residence time of the carbon phases are strongly coupled to f_{O_2} (Bryndzia and Wood, 1990; Luth, 1993; Stagno *et al.*, 2015). Thermodynamics predictions of the redox profile of the subducting slab show that at oxidizing conditions at depth of 100km ($f_{O_2} > \sim \text{FMQ} - 1$, i.e., 1 log unit below the fayalite-magnetite-quartz oxygen fugacity buffer) the mobile species, such as CO₂ fluid or carbonatite melt, are stable; at relatively low f_{O_2} ($f_{O_2} < \sim \text{FMQ} - 1$), the immobile carbon species, diamond or graphite, are stable; while at extremely reduced conditions ($< \sim \text{FMQ} - 3$), the carbon species within the C-O-H fluid system are mobile again as hydrocarbon-rich fluid (Frost, 1979; Matveev *et al.*, 1997; Frost, 2012; Stagno *et al.*, 2015). Carbon can enter subduction zones in the form of minor biotic organic matter, sedimentary carbonate, and altered carbonates in the crust (Staudigel *et al.*, 1989; Alt and Teagle, 1999; Plank, 2014). The most biotic organic matter may decompose or be exhausted by metamorphic reaction with oxidized matter (e.g. Fe-Mn oxides) before subduction proceeds (Claypool and Kaplan, 1974; Froelich *et al.*, 1979). The stability of polymerized fluids, indeed, has been reported in literature either from evidences in natural rocks (Frezzotti *et al.*, 2011), or by thermodynamic calculations that take into account the solubility behavior of silicate minerals in water-rich fluids at mantle conditions (Sverjensky *et al.*, 2014) as a function of pressure, temperature and oxygen fugacity. Further theoretical predictions and experimental simulations showed these hydrocarbon fluids are immiscible in the subduction environments (Huang *et al.*, 2017; Li *et al.*, 2017). However, to

date, limited natural observations were confirmed for the formation of abiotic hydrocarbons in the subduction environments.

The formation of the abiotic hydrocarbons in nature provides a unique window into our understanding of organic-inorganic interactions. It is well documented that most known natural hydrocarbons are of biogenic origin. However, there are several recent reports that have demonstrated that some hydrocarbons, particularly methane and other light hydrocarbons, were derived from abiotic precursors in various geological settings related to deep processes (Etiope and Schoell, 2014, and references therein). Abiotic alkanes have been found in the Earth's lower crust (Lollar *et al.*, 2002) and the Precambrian Shields (Lollar *et al.*, 2008). Abundant abiotic methane (CH₄) has also been found in orogenic harzburgite rocks of the Early Paleozoic suture zone in northwestern China (Song *et al.*, 2009), and in natural diamonds from Congo and Brazil (Melton and Giardini, 1974). More intriguingly, hydrocarbon-bearing fluid inclusions have been widely observed in metamorphic rocks from subduction zones, such as the Dabie-Sulu terranes in eastern China, the jadeite tract in Myanmar, the Sanbagawa belt in Japan, the Raspas Complex in Ecuador, and Alps belts in Italy (Fu *et al.*, 2003; Shi *et al.*, 2005; Arai *et al.*, 2012; Herms *et al.*, 2012; Brovarone *et al.*, 2017). For these hydrocarbons observed in metamorphic rocks from subduction zones, it is still hard to distinguish whether they are abiotic or not, because normally only tiny amounts of hydrocarbons are trapped as fluid inclusions in metamorphic minerals.

Here, we report the presence of light hydrocarbon-bearing fluid inclusions and graphite in the carbonated eclogites from the S.W. Tianshan UHP oceanic subduction zone. The observed light hydrocarbon-bearing inclusions and graphite likely results from an abiotic reduction of Fe-bearing carbonate and metamorphic fluids, supported by the low oxygen fugacity constrained by the coexisting minerals. Furthermore, high-pressure experiments in the system containing iron-

bearing dolomite (ankerite) and water were carried out to provide additional support for the formation of abiotic light hydrocarbons from carbonate reduction under subduction settings.

2. Geological setting and sample descriptions

2.1 Geological setting

Composed of marble, metapelite, blueschist, eclogite, and serpentinite, the Chinese Tianshan orogenic belt extends for more than 200 km between the Tarim plate and the Yili-central Tianshan plate (Fig. 1). It is the world largest known oceanic (U)HP metamorphic orogen, confirmed by quartz exsolution lamellae in omphacite (Zhang *et al.*, 2002a), residual magnesite in dolomite in eclogite (Zhang *et al.*, 2002b), coesite in the eclogite and metapelite (Lü *et al.*, 2008; Yang *et al.*, 2013), decomposition structure of dolomite in eclogite and metapelite (Zhang *et al.*, 2003; Tao *et al.*, 2014), and Ti-chondrodite- and Ti-clinohumite-bearing serpentinitized ultramafic rocks (Shen *et al.*, 2015). Maximum metamorphic pressure-temperature conditions are constrained to ~ 3 GPa and ~ 600 °C by phase equilibrium calculations and petrological occurrence of coesite (Lü *et al.*, 2009; Tian and Wei, 2012). Metamorphic basalt with pillow structure and MORB/OIB-like geochemical characteristics indicates the S.W. Tianshan is a typical oceanic subduction orogenic belt (Ai *et al.*, 2006; Xiao *et al.*, 2012).

2.2 Sample descriptions

Carbonation (5-30 vol.%) is very common in most (U)HP meta-ophiolites (e.g. carbonated metapelite, carbonated eclogite and carbonated serpentinite) from the S.W. Tianshan subduction orogen (Zhang *et al.*, 2002b; Zhang *et al.*, 2003; Lü *et al.*, 2013; Li *et al.*, 2014; Tao *et al.*, 2014; Shen *et al.*, 2015). Dotted graphites are dispersed in all kinds of meta-ophiolites (e.g., metapelite and marbles) from S.W. Tianshan subduction zones (Lü *et al.*, 2013). These large amounts of carbon-bearing phases (e.g. carbonate and graphite) in different meta-ophiolite after (U)HP metamorphism from the S.W. Tianshan subduction belt is important sources of carbon recycled

into the deep Earth, and it makes ideal samples for studying the deep carbon cycle in subduction zones (Tao *et al.*, 2014). We have petrologically and geochemically characterized tens of carbonated eclogite samples from the S.W. Tianshan subduction zone in previous studies (Tao *et al.* 2014; Tao *et al.*, 2018a). In this study, three carbonated eclogites (315-3, H608-23 and K949) were selected to investigate possible formation and preservation of abiotic hydrocarbons in the S.W. Tianshan subduction zone. Their locations are marked with red stars on the schematic geological map (Fig. 1). All three samples were collected in the same drainage areas of the Habutengsu River.

3. Methods

3.1 Petrological analyses

Petrological studies are carried out on carbonated eclogites with optical microscopy, Raman spectroscopy, scanning electron microscopy (SEM), and electron probe microanalysis (EPMA). Raman spectra from 100 to 1600 cm^{-1} were collected on carbon-bearing phases (carbonates, graphite, and fluid inclusions) in carbonated eclogites at ambient condition by using a confocal micro-Raman spectroscopy (Renishaw system RM-1000; 514.5 nm Ar-ion laser operating at 20 mW; back-scattering geometry; 60 s counting time). Backscatter Electron (BSE) images were collected on thin sections without carbon coating by using an FE-SEM (Quanta 650 FEG; low vacuum mode and 15 kV), and chemical compositions of the mineral phases in the carbonated eclogites were determined with carbon-coated thin sections by using a JEOL JXA-8900R electron microprobe. Synthetic silica (Si) and spessartine (Mn), natural pyrope (Mg, Al), andradite (Fe, Ca), albite (Na), rutile (Ti) and sanidine (K) were used as standards. A ZAF correction program was used to reduce final results. The bulk compositions of the carbonated eclogites were obtained by X-ray fluorescence (XRF). All petrological analyses in this study

were conducted at the MOE Key Laboratory of Orogenic Belt and Crustal Evolution at Peking University.

3.2 Measurement of Fe^{3+} in garnet using the “Flank method”

Garnets containing both Fe^{3+} and Fe^{2+} are potentially sensors of f_{O_2} in metamorphic rocks from subduction zones and in garnet peridotite from the mantle (Luth *et al.*, 1990; Woodland and O'Neill, 1993; Stagno *et al.* 2013; Stagno *et al.*, 2015). To constrain the oxygen fugacity of the S.W. Tianshan subduction zone, the Fe^{3+} concentrations in eclogitic garnet were measured by the “Flank method” with the electron microprobe (Höfer and Brey, 2007). The $\text{Fe}^{3+}/\Sigma\text{Fe}$ ratio profile of garnet in carbonated eclogite (K949) was measured from core to rim by the “Flank method” at the microprobe laboratory of Institut für Geowissenschaften, Mineralogie, Goethe-Universität, where the “Flank method” was developed (Höfer *et al.*, 1994). Höfer and Brey (2007) determined the iron oxidation state of garnet with the “Flank method” and yielded as precise and accurate results as Mössbauer spectroscopy. For this study, the “Flank method” was calibrated on a JEOL JXA 8900RL microprobe. The $\text{FeL}\alpha$ and $\text{L}\beta$ intensities were measured for a fixed counting time of 300s each at 15 kV and 200 nA. The iron metal $\text{L}\alpha$ line was used to optimize the PHA conditions (in differential mode) for the measurement of $\text{FeL}\alpha$ and $\text{L}\beta$ intensity. One spectrometer with a TAP crystal and smallest detector slit (300 μm) were used for the “Flank method” measurements. The remaining 4 spectrometers simultaneously carried out quantitative analyses of 12 elements (Si, Ti, Al, Cr, Fe, Mn, Ni, Mg, Ca, Na, K, P) with appropriate standards, e.g., pyrope (Mg, Si), almandine (Fe), MnTiO_3 (Mn, Ti), CaSiO_3 (Ca), and garnets with variable total Fe and $\text{Fe}^{3+}/\Sigma\text{Fe}$ known from Mössbauer “milliprobe” (McCammon *et al.*, 1991). The garnet $\text{Fe}^{3+}/\Sigma\text{Fe}$ ratio was determined with the “Flank method” by correcting for self-absorption. The detailed procedure of the “Flank method” measurement of the $\text{Fe}^{3+}/\Sigma\text{Fe}$ ratio in garnets is described in the publication by Höfer and Brey (2007) and Tao *et al.*, (2018b). In order to

increase the intensity of the FeL α and L β emission and for a better statistically based precision, we used the higher probe current of 200 nA in this study compared to the first calibration of the “Flank method” by Höfer and Brey (2007). In addition, the major chemical compositions (e.g. Si, Ti, Al, Cr, Fe, Mn, Ni, Mg, Ca, Na, K) of the garnets and their inclusions (e.g. omphacite) were analyzed by EPMA to be able to calculate the oxygen fugacity conditions of carbonated eclogites from the S.W. Tianshan subduction zone using the garnet-clinopyroxene oxybarometer (Stagno *et al.*, 2015).

3.2 Thermodynamical constraint of P-T- f_{O_2} evolution

Thermodynamic phase equilibrium modeling is a common method for reconstructing PT condition of metamorphic rocks. In this study, we calculated pressure and temperature conditions of carbonated eclogite (K949) from S.W. Tianshan subduction zone by phase equilibria modelling in the system of MnO - Na₂O - CaO - K₂O - FeO - MgO - Al₂O₃ - SiO₂ - H₂O - O - CO₂ (MnNCKFMASHO-CO₂) considering the mineral assemblages and bulk compositions. The bulk-rock chemical compositions of carbonated eclogite (K949) for pseudo-section calculation was normalized in the MnNCKFMASHO system. Quartz/coesite is considered in excess because ubiquitous quartz was observed in the thin section. TiO₂ and P₂O₅ are neglected as they are mainly present as rutile/ilmenite and apatite accessory phases. 5 wt.% of carbonate (similar to optical observation) was included in the system as representative of the stability of carbon-bearing phases in the carbonated eclogites. The molar amount of CO₂ + H₂O was set to be in excess, which is consistent with fluid-saturated conditions in the cold subduction zones (Okamoto and Maruyama, 1999). P-T pseudosections were calculated using the software THERMOCALC 3.33 (Holland *et al.*, 1998) with the updated version of the dataset (Holland and

Powell, 1998). Activity-composition relationships of metamorphic minerals (e.g. garnet, omphacite) are taken as in a previous study (Tian and Wei, 2012). Lawsonite, aragonite, calcite and quartz/coesite were treated as pure end-member phases. The chemical composition profile of garnets from the carbonated eclogite (K949) was plotted on the isopleths of garnet end-members in the pseudo-section phase diagram to constrain the P-T evolution trend of S.W. Tianshan subduction zone.

The redox chemical equilibrium, $5\text{CaFeSi}_2\text{O}_6$ (hendenbergite) + $1/3\text{Ca}_3\text{Al}_2\text{Si}_3\text{O}_{12}$ (grossular) + $\text{O}_2 = 2\text{Ca}_3\text{Fe}_2\text{Si}_3\text{O}_{12}$ (andradite) + $1/3\text{Fe}_3\text{Al}_2\text{Si}_3\text{O}_{12}$ (almandine) + 4SiO_2 (coesite) (Stagno *et al.*, 2015) was used that requires the knowledge of Fe^{3+} content of garnet to calculate the $f\text{O}_2$ evolution of carbonated eclogite (K949). The thermodynamic data used for the equation are from Holland and Powell (2011). The activity-composition relations for garnet solid solution were modified from Gudmundsson and Wood (1995). The Fe^{3+} content of the garnets from the “Flank method” was used to calculate the activity of grossular ($\text{Ca}_3\text{Al}_2\text{Si}_3\text{O}_{12}$), almandine ($\text{Fe}_3\text{Al}_2\text{Si}_3\text{O}_{12}$) and andradite ($\text{Ca}_3\text{Fe}_2\text{Si}_3\text{O}_{12}$) end-members of garnet. The oxygen fugacity evolution trend of carbonated eclogite (K949) was constrained by the paired garnet host and omphacite inclusion formed at different metamorphic stages.

The $f\text{O}_2$ of carbonated eclogite (H608-23) was also thermodynamically constrained by the coexisting ankerite, calcite, magnetite, and graphite assemblages in the CaO-FeO-H₂O-CO₂ system. The pressure- $f\text{O}_2$ phase diagram was thermodynamically calculated in the CaO-FeO-CO₂-O system at 550 °C to constrain the $f\text{O}_2$ at which Fe-bearing carbonate (ankerite) was reduced to magnetite and graphite using the ThermoCalc program with the improved thermodynamic dataset (Holland and Powell, 2011).

3.3 High-pressure experiment simulation

In order to further explore the abiotic formation of hydrocarbon-bearing fluid inclusions and graphite in the carbonated eclogite, we have designed and conducted a series of experiments on the reaction of Fe-bearing dolomite (ankerite) plus water under typical pressure-temperature conditions of subduction zones and upper mantle. Previous experiments have focused on the formation of graphite and light hydrocarbon fluid from carbonate reduction at relatively low pressures at MPa ranges (e.g., Giardini and Salotti, 1969; McCollom, 2003; Milesi *et al.*, 2015). In this study, we have extended these experiments to pressures between 1 and 6 GPa at temperatures of 600-1200 °C using a piston-cylinder apparatus and a large cubic press.

3.3.1 Experimental conditions

Natural ankerite was used as starting material. Its chemical composition, $\text{Ca}_{1.02}(\text{Fe}_{0.52}\text{Mg}_{0.43}\text{Mn}_{0.04})(\text{CO}_3)_2$, was confirmed with a JXA-8900 microprobe at the Geophysical Laboratory (Carnegie Institution of Washington). For the high-pressure experiments, two different diameters of gold capsules were used, 2.5 mm and 5 mm in diameter respectively. Beforehand, the capsule was crimped, sealed at one end by arc welding, boiled twice in diluted HCl (30 min at 250 °C), and ultrasonically cleaned in distilled water (20 min) to thoroughly remove possible organic matter. We first loaded ~ 10 weight % distilled water to the bottom of the capsule, and then loaded the ankerite powder, that means the water/rock weight ratio is ~ 1:9. The loaded capsule, surrounded by wet tissue, was quickly sealed by arc welding.

High-pressure experiments were carried out at the High-Pressure and High-Temperature Laboratory, Peking University (PKU) (Liu *et al.*, 2012a). Experiments below 2 GPa were carried out using the Quick Press piston-cylinder apparatus, while experiments above 3 GPa were performed using a CS-IV 6×14 MN cubic press. Details of the cell assemblies and calibrations

for piston-cylinder apparatus and cubic press were described in previous publications (Liu *et al.* 2012a; Liu *et al.* 2012b). The pressure uncertainties, which depend largely on the accuracy of the calibration reaction, were estimated to be less than 5% (Liu *et al.*, 2012a). The experimental temperature was measured and controlled with a Pt₉₄Rh₆-Pt₇₀Rh₃₀ thermocouple (type B), ignoring the pressure effect on its e.m.f.. Both pressure and temperature were automatically controlled during the experiments. The sample was first pressurized to the target pressure, and then heated at a rate of 100 °C/min. Experiments were quenched by turning off the power, followed by automatic decompression to ambient pressure. From recording temperature with the thermocouple, we found that all experiments were quenched to below 100 °C within 10 seconds. The effect of quenching process on the gaseous phases in the capsule is not discussed here because it is beyond the scope of this study.

The experiments were conducted at higher temperatures (> 600 °C) than the conditions of the natural ultra-high-pressure metamorphic rock (<600 °C) to ensure that chemical equilibrium could be achieved over a reasonable duration of the laboratory experiment. Time-series experiments (A-C-2, A-C-3, and A-C-4) were performed at 1.5 GPa and 1000 °C to evaluate phase equilibrium. No significant change in the iron content in the recovered ankerite was observed after a couple of hours, indicating that experiments can reach equilibrium within a couple of hours. Therefore, all other experiments were performed for more than 24 hours, which should be sufficiently long to reach equilibrium.

3.3.2 Analyses of experimental products

In order to determine the composition of the gas phases, we collected the gases from the quenched gold capsule using either a piercing device or a crushing device connected to an Agilent 6890A gas chromatograph (GC). The gas chromatograph technique provides definitive

identification and quantitative measurement of the hydrocarbons and other gas phases present in the sample with high sensitivity. The gold capsule recovered from the high-pressure experiment was punched with a hard steel needle. The entire capsule was loaded in the valve chamber below the steel needle. We sealed one end of the valve and connected the other end to the GC. The valve chamber was evacuated to high vacuum. We then broke the capsule by rotating the valve handle, and extracted the gases in the capsule to the GC chamber. In most cases, we cannot completely extract gases in the capsule by piercing device because gases may be trapped in the sample. In order to completely extract gases, we loaded the capsule after the piercing method into a small iron tube chamber with one end sealed, and another end connected to the GC. The iron tube chamber was evacuated to high vacuum, and we then crushed the iron tube with a small hand press to extract rest of the gases from the run products to the GC. The details of the analytical method were previously published (Pan *et al*, 2006). Measurements were performed with an Agilent 6890A gas chromatograph (modified by Wasson ECE Instrumentation) at the State Key Laboratory of Organic Geochemistry, Guangzhou Institute of Geochemistry (Chinese Academy of Sciences). Before each measurement of the extracted gases by the gas chromatograph, we collected the background GC pattern of the instrument to ensure no contamination. The GC analyses were only carried out with the larger recovered samples (~180 mg) from experiments with the 5 mm gold capsule diameters to ensure sufficient amounts of gas phases in the run products for reliable gas content measurements.

After measurement of the gas phases in the capsule using GC, the samples were cut out from the capsule for further analyses. To identify solid phases of the run products, the recovered sample was mounted in epoxy resin and polished for analyses with Raman Spectroscopy, scanning electron microscopy (SEM) and electron probe microanalysis (EPMA). All analyses

were performed at the same apparatus and same conditions as described above (Part 3.1) at the MOE Key Laboratory of Orogenic Belt and Crustal Evolution, Peking University.

4. Results

4.1 Petrological observation

4.1.1 Mineral assemblages

The mineral assemblages of carbonated eclogites consist of similar garnet porphyroblasts, fine-grained omphacite matrix, along with varying amounts of accessory minerals including carbonate, muscovite, paragonite, glaucophane, epidote, phengite, quartz, and rutile/ilmenite, observed under optical microscope. Poikilitic porphyroblasts of garnets always contain inclusions of omphacite, zoisite, carbonates, and rutile. Subhedral carbonates are dispersed in the matrix or found as inclusions in garnets. The petrographic and geochemical characteristics of carbonated eclogites from S.W. Tianshan subduction zone has been well described in our previous studies (Tao *et al.*, 2014; Tao *et al.*, 2018a).

In this study, we focus on the P-T- f_{O_2} evolution trend of the S.W. Tianshan subduction zone constrained from the metamorphic mineral assemblages in the carbonated eclogites. In sample K949, different omphacite inclusions were observed in garnet from the core to the rim (Fig. 2a and Table S1). The coexisting garnet and omphacite at different metamorphic stages can be used to constrain a f_{O_2} evolution trend using garnet and omphacite oxybarometer (Fig. 2d). The P-T evolution trend can also be constrained by a compositional profile of garnet and equilibrated mineral assemblages (Fig. 2a). In sample H608-23, no omphacite was observed in garnet porphyroblasts in the thin section (Fig. 3c). Although some matrix omphacites were observed in

equilibrium with garnet (Fig. 3a), it is hard to assign the f_{O_2} from garnet porphyroblast and matrix omphacite to different metamorphic stage. However, in sample H608-23, we observed the reduction reaction from Fe-dolomite to coexisting graphite and magnetite in the matrix (Fig. 3c), which can be used to constrain the f_{O_2} condition at which the Fe-bearing carbonate was reduced to graphite and magnetite in carbonated eclogite (Fig. 3d). The mineral assemblages of Fe-dolomite, graphite and magnetite were confirmed by typical Raman spectra (Fig. 3b). Remnant of fluid-pockets with deposited graphite was observed in H608-23 (Fig. 3c). The Fe-dolomite in H608-23 shows a slight variation [$Fe^{\#} = Fe/(Fe + Mg)*100$] ranging from 6 to 10 in Fe concentration (Fig. S1). In carbonated eclogite (315-3), garnet porphyroblast and omphacite matrix are predominant minerals with small amounts of rutile and carbonate (Fig. 4a). Some omphacite and minor rutile were also observed in garnet porphyroblast, too.

4.1.2 Mineral chemistry

Garnets from carbonated eclogite (K949) show compositional and $Fe^{3+}/\Sigma Fe$ ratio zonation from the core to the rim (Table 1 and Fig. 2b), which can be used to reveal the P, T and f_{O_2} evolution of carbonated eclogites from S.W. Tianshan subduction zone. These garnets show an increase of pyrope and decrease of almandine from the core to the rim, and a slight decrease of grossular and spessartine from the core to the rim (Table 1 and Fig. 2b). The increase of pyrope coupled with the decrease of grossular and spessartine in garnet from core to rim indicate a typical prograde metamorphism. The $Fe^{3+}/\Sigma Fe$ ratios of garnet profiles in K949 by “Flank method” show a slight decrease from 0.050 to 0.026 from core to rim (Table 1 and Fig. 2b). Na-clinopyroxenes are classified to omphacite in both garnet and matrix according to Morimoto *et al.*, (1988) (Table S1). Amphiboles are glaucophane and barroisite according to the Na-amphibole classification (Leake *et al.*, 1997) (Table S1). The glaucophane porphyroblasts in

matrix usually contain inclusions of omphacite, rutile, and carbonate, indicating their formation during the retrograde stage. Phengite/paragonite flakes in the carbonated eclogite are oriented in parallel with the dominant foliation of the specimen. The chemical compositions of typical metamorphic minerals from carbonated eclogites H608-23 and 315-3 are listed in Table S2 for comparison.

4.1.3 Hydrocarbon fluid inclusions

Abundant fluid inclusions were also found in the high-pressure omphacite in sample 315-3 (Fig. 4a), which coexists with garnet. The coexisting garnet also contains tiny fluid inclusions (typically $< 2 \mu\text{m}$). Light hydrocarbons (methane and ethane) were identified in omphacite grains (Fig. 4b). The Raman spectrum of the inclusion bubble in omphacite (Fig. 4c and d) shows characteristic CH stretches at around 2917 cm^{-1} . The observed peak seems to be too broad to be due to the symmetric stretch band of methane alone at 2917 cm^{-1} (cf. Lin *et al.*, 2007). The broad feature is consistent with the additional contribution from the intense doublet of ethane at 2895 cm^{-1} and 2955 cm^{-1} (e.g., Atamas *et al.*, 2004), shown as the shoulders on both sides of the 2917 cm^{-1} methane peak, marked with a tick in Fig. 4c and d. The broad peak at 3440 cm^{-1} is due to the OH stretch. Only the OH stretch was detected in the fluid phase (Fig. 4c and d), indicating H_2O -dominated fluid inclusion with low gas solubility. All peaks at wavenumbers below 1200 cm^{-1} can be indexed based on the Raman spectrum of omphacite with the most intense peak at 681 cm^{-1} (Fig. 4c and d).

The fluid inclusions in omphacite with non-planar populations are tubular with their long dimension parallel to the c-axis of the omphacite crystals (Fig. 4b). These features suggest that they are primary inclusions trapped during the growth of omphacite at the high-pressure metamorphic event (Gao and Klemd, 2001). They are also characterized by low salinity (~ 4

wt% NaCl equivalent), estimated from freezing-point depression using the Linkam THMS600 heating and freezing stage. The likely carbon source of the fluid inclusions is from predominant carbon-bearing phases (carbonate) in carbonated eclogite. Similar fluid inclusions (no hydrocarbon) associated with daughter carbonate were reported in eclogite from S.W Tianshan subduction zone (see Fig. 4 in Gao *et al.*, 2007).

4.1.4 P - T - f_{O_2} evolution

The calculated pseudosection for carbonated eclogites (K949) using bulk-rock composition is contoured with isopleths of grossular and pyrope contents in garnet (Fig. 2c). In the possible mineral assemblage region, the grossular content decreases obviously with an increase of pressure, while the pyrope content increases with an increase of temperature. The chemical composition profiles of two garnet grains in K949 were plotted on the thermodynamic pseudosection to constrain the metamorphic P-T path of this carbonated eclogite (gray belt in Fig. 2c). Garnet compositions were plotted in the dolomite- and glaucophane- bearing lawsonite eclogite region, which is consistent with the mineral assemblages observed by optical microscopy (Fig. 2a). The slight decrease of grossular profile indicates almost isobaric process (at ~ 25 kbar), while the obvious increase of pyrope content indicates a heating process from ~500 to ~575 °C (Fig. 2c). In other words, the garnet profiles in K949 record an isobaric heating prograde process (gray belt in Fig. 2c).

Omphacite inclusions at different metamorphic stages were observed in garnets from mantle to rim in K949 (Fig. 2a and Table 1). Along the garnet growing zonation, we chose three garnet-omphacite pairs to constrain the oxygen fugacity evolution trend using equilibrium: $5CaFeSi_2O_6$ (clinopyroxene) + $1/3Ca_3Al_2Si_3O_{12}$ (garnet) + $O_2 = 2Ca_3Fe_2Si_3O_{12}$ (garnet) + $1/3Fe_3Al_2Si_3O_{12}$ (garnet) + $4SiO_2$ (coesite) (Stagno *et al.*, 2015). The calculated P-T conditions were used to calculate the oxygen fugacities. We calculated the oxygen fugacities at 500, 550, 575 °C and ~ 25 kbar using

the garnet-omphacite oxybarometer for K949 (Fig. 2d). The constrained oxygen fugacities were corrected for the presence of quartz, rather than coesite which implies a correction of ~ -0.3 log units. These f_{O_2} showed a decrease from FMQ-1.89 to FMQ-2.46 via FMQ-2.09 falling into the graphite stability field (Fig. 2d). Garnet and its omphacite inclusions in K949 recorded a decreased oxygen fugacity during the prograde isobaric heating process.

We observed the reduction structure of Fe-bearing dolomite into aragonite, magnetite, and graphite in the carbonated eclogite (H608-23) (Fig. 3c), which was used to constrain the f_{O_2} . Figure 3d shows the estimated oxygen fugacity from the reduction reaction of Fe-bearing dolomite into aragonite, magnetite, and graphite. The upper bound of the oxygen fugacity for the carbonated eclogite H608-23 is constrained by the reaction of ankerite = calcite + magnetite + graphite + O_2 ($ACMG_{H608-23}$, blue line in Fig. 3d). The activity of ankerite ($\alpha_{Ank} = 0.34$) is determined on the basis of microprobe analyses of the composition of Fe-bearing dolomite according to the solid solution model of dolomite and ankerite (White *et al.*, 2003). The calculated value (blue line) is lower than QFM buffer (red line) by about 1.5 log units (Fig. 3d). The f_{O_2} ($< \sim FMQ-1.5$) constrained for reduction of carbonate to graphite in the carbonated eclogite in this study is very consistent with recent experimental work (see Fig. 8 in Stagno *et al.*, 2015)

4.2 High-pressure experimental results

Table 2 lists the experimental conditions and the observed phases in the recovered samples. We have observed a number of hydrocarbons including methane, ethane, and propane in all of the recovered samples (Table 3). Figure 5 shows a representative gas chromatogram with a flame ionization detector, indicating the presence of CH_4 , C_2H_6 , and C_3H_8 in the recovered sample (A-C-7). Table 3 shows the measured gas contents for all of the large samples (5-mm capsule). The

efficiency of extracting gas phases from run products depends on the interconnectivity of the pores and fracture distribution in the quenched samples. The needle-piercing method yielded extremely high values for CO₂ gas. The total amounts of gases extracted from the piston-cylinder experiment is relatively high, especially in which siderite was also observed, but very low values for the total amounts of gases extracted from the multi-anvil experiments (Table 3). The difference could indicate significant differences in pore distribution and fractures between the recovered piston-cylinder and multi-anvil samples. For the multi-anvil samples, the needle-piercing method alone produced very low yields of the gas phases (< 0.005 mL). Therefore, the measured values and ratios are less reliable. A combination of piercing and crushing of the entire sample significantly increased the efficiency of gas extraction, yielding about 10 times more gases released from the samples (~ 0.05 mL) and producing more consistent results on the gas extraction. The emphasis of the analyses is on positive identification of the gas phases in the run products for this study. It is difficult to assess the full production of the gas phases because of possible incompleteness of gas extraction and unknown initial water content. However, the ratios of different gases may provide some insights into the general trends of gas production as functions of oxygen fugacity, pressure, and temperature. CO₂ is the dominant gas in all the recovered samples, accounting for more than 96 % of the total measured gases. Among the detected hydrocarbons, methane is always the dominant hydrocarbon component although considerable amounts of ethane and propane were also detected in the run A-C-6 recovered from 4 GPa and 1200 °C (Table 3). Coincidentally, this run also showed the lowest Fe# in the recovered ankerite among the large-capsule experiments (Table 2).

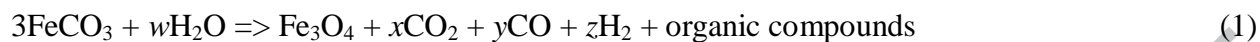
All experiments at pressures from 1 to 6 GPa at 600-1200 °C produced the solid phase assemblage including ankerite (Ank), graphite (Gr), and magnetite (Mgt) (Table 2). The

recovered samples from low pressure (< 2 GPa) experiments contain many relatively large voids (up to $50\mu\text{m}$), partially filled with graphite (Fig. 6). The voids must have been filled with fluid/gas phases together with graphite during the experiments. Fluid inclusions in ankerite were easily identified by the optical microphotograph (Fig. 6c), and Raman spectra of the fluid inclusions were collected. Figure 6d shows a representative Raman spectrum of the fluid inclusion, which shows the characteristic CH stretches at around 2917 cm^{-1} together with the peaks of graphite and ankerite. The Raman spectrum in the CH stretch region is very similar to that of the natural fluid inclusion. We interpret the broad feature of the Raman peak as the result of contributions from the methane symmetric stretch band at 2917 cm^{-1} together with the doublet of ethane at 2895 cm^{-1} and 2955 cm^{-1} . The presence of methane and ethane in the synthetic fluid inclusion is further supported by independent measurements using gas chromatography. Presence of graphite in the run products was confirmed on the Raman spectra and EDS elemental mapping (Fig. 6a and d), indicating a graphite-saturated fluid. The solid phase assemblage of ankerite, magnetite, and graphite is also confirmed by X-ray diffraction measurements and with SEM (scanning electron microscope) analyses (Fig. 5b). The Fe content in the recovered ankerite is lower than that of the starting material, indicating loss of iron to form magnetite (Table 2). The Fe contents of the starting material Fe-dolomite generally decrease with both time (Fig. S2a) and temperature (Fig. S2b), which is comparable with that from naturally carbonated eclogite (H608-23; Fig. S1).

4.3 Formation reaction for abiotic hydrocarbons

McCullom (2003) experimentally studied the siderite (FeCO_3) decomposition in the presence of water vapor at $300\text{ }^\circ\text{C}$ and ambient pressure, and generated a variety of organic

products dominated by alkylated and hydroxylated aromatic compounds. The overall reaction for synthesis of the hydrocarbons from siderite is suggested as:

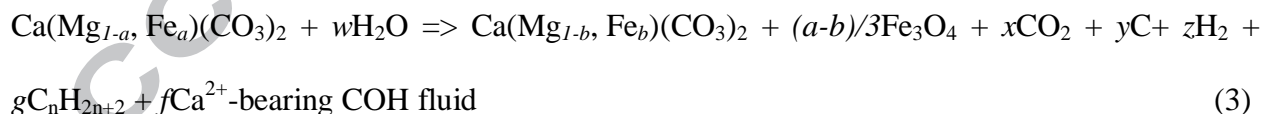


where w , x , y , and z are undetermined stoichiometric coefficients.

A similar reaction was suggested by Milesi *et al.* (2015) as



from an experimental study of the system siderite and water at 200 and 300 °C under a pressure of 50 MPa. In our study, the predominant carbonate observed in natural eclogites from S.W. Tianshan subduction zone is Fe-bearing dolomite (ankerite): $\text{Ca}(\text{Mg}_{1-a}, \text{Fe}_a)(\text{CO}_3)_2$, where a is $\text{Fe}/(\text{Fe}+\text{Mg})$ in the dolomite. Similar Fe-bearing dolomite was used as the starting material for the high-pressure simulations in this study. The oxidized iron (Fe_3O_4) and reduced carbon species (e.g. graphite and hydrocarbons) were documented in both field specimen and the recovered experimental charges. Also, a variety of Fe concentrations in Fe-bearing dolomite was observed in both natural and experimental samples in our study. Based on previous low-T and low-P experiments (McCollom, 2003; Milesi *et al.*, 2015), and petrological observation and high-P experimental simulation in our study, the possible chemical reaction for the formation of hydrocarbons can be written as:



where a and b are $\text{Fe}/(\text{Fe}+\text{Mg})$ of starting and product Fe-bearing dolomite, a is greater than b in this study, and w , x , y , z , g , and f are undetermined stoichiometric coefficients.

The starting material for our experiments is natural Fe-dolomite (Ankerite). Its chemical formula is $\text{Ca}_{1.02}(\text{Fe}_{0.52}\text{Mg}_{0.43}\text{Mn}_{0.04})(\text{CO}_3)_2$. The initial $\text{Fe}^\# = [\text{Fe}^{2+}/(\text{Ca}+\text{Mg}+\text{Fe}^{2+}+\text{Mn})] \times 100$ of the

starting material is 26 (Table 2). After the experiments, the $Fe^{\#}$ of ankerite in the run products decreased to a value as low as 8. This indicates that the $FeCO_3$ component in $Ca_{1.02}(Fe_{0.52}Mg_{0.43}Mn_{0.04})(CO_3)_2$ is the fundamental reactant for the redox reaction. The mechanism of the redox reaction is similar to McCollom (2003) and Milesi *et al.*, (2015) except that the activity of the $FeCO_3$ component in $Ca_{1.02}(Fe_{0.52}Mg_{0.43}Mn_{0.04})(CO_3)_2$ is depending on the activity model and chemical composition of the ankerite. The dissolved Ca and Mg cations in the fluid may also have some effect on the synthesis of abiogenic hydrocarbons at high PT conditions (McDermott *et al.*, 2016).

5. Discussion

5.1 Decreased fO_2 of the subduction zone and its effect on the deep carbon cycle

The fO_2 of the asthenospheric mantle below mid-ocean ridges was constrained by the oxybarometer of abyssal peridotites (Bryndzia *et al.*, 1989) and $Fe^{3+}/\Sigma Fe$ ratios of MORB basaltic glass (Bézos and Humler, 2005) to be close to FMQ-1 (Christie *et al.*, 1986; Frost and McCammon, 2008). However, the fO_2 of the mantle wedge above subducting slabs, whose fO_2 is always from FMQ to FMQ+2, including substantial proportion with $fO_2 > FMQ+1$, is often summarized as being more oxidized than asthenospheric mantle (Frost and McCammon, 2008 and references therein). These more oxidized values are usually attributed to the addition of more oxidizing matters (e.g. H_2O) from subduction zones (Parkinson and Arculus, 1999; Wood and Virgo, 1989; Bezos and Humler, 2005; Malaspina *et al.*, 2009; Kelley and Cottrell, 2009). Therefore, a relatively oxidized condition for subduction zones is generally proposed. However, until now, only few studies constrained the real in situ fO_2 of a subduction zone because the oxygen fugacity of the subduction zone is complex (Foley, 2011). Metamorphic rocks in the

subduction zone always have a wider range of possible fO_2 values than most igneous rocks. Meanwhile, at different metamorphic stages in the subduction zone, the oxygen fugacity varies a lot (Donohue and Essene, 2000).

The oxidation state of initial oceanic MORB slabs (FMQ-1) is affected by hydrothermal alteration (e.g. hydration) and sedimentation before entering the subduction zone. Normally, the oxidation state of altered oceanic crust before subduction is estimated between FMQ-1 and FMQ (Foley, 2011). Subduction of altered oceanic crust, which is metamorphosed to (carbonated) eclogites at pressure > 1 GPa, is the major mechanism by which carbon enters the mantle. The fO_2 evolutions of subducting slabs should have a significant effect on the stability and speciation of carbon-bearing phases in subduction environments (Aulbach and Stagno, 2016). In this study, we constrained the fO_2 evolution trend of S.W. Tianshan subduction zones by different oxybarometers in situ. Figure 7 shows the fO_2 of the S.W. Tianshan subduction zone, compared with those in other geological environments. A slightly decreased fO_2 (from FMQ - 1.9 to FMQ - 2.5) was recorded for prograde metamorphism of the S.W. Tianshan subduction zone using the garnet-omphacite oxy-barometer. This low fO_2 range is also consistent with the low oxygen fugacity ($< \sim$ FMQ - 1.5) constrained by the observed reduction reaction from Fe-bearing dolomite to calcite, magnetite, and graphite. In comparison with the oxygen fugacity of DQDG (dolomite + 2 quartz = diopside + 2 graphite + 2O₂) in Fig. 7, which controls the formation of graphite from the reduction of carbonate in carbonated eclogite assemblages (Luth 1993; Stagno *et al.*, 2015), the oxygen fugacity of S.W. Tianshan is relatively low. This is consistent with ubiquitous graphite in meta-ophiolites from S.W. Tianshan subduction zone (Lü *et al.*, 2013). Further, the C-H₂O oxygen fugacity buffer, separating CH₄- and CO₂-rich aqueous fluid ($X_{O_2}=1/3$), was also shown (C-H₂O in Fig. 7), calculated using the COH model (Zhang and Duan,

2009). Below this boundary, abiotic hydrocarbon will form from C-H-O fluid. This is another constraint for the formation of abiotic hydrocarbon in the S.W. Tianshan subduction zone. The observed oxygen fugacity of the S.W. Tianshan subduction zone is also comparable to that of the Alpine Corsica where the abiotic production of reduced graphite in subduction zones during decarbonation was suggested (Galvez *et al.*, 2013; Malvoisin *et al.*, 2011). An increased retrograde fO_2 (FMQ + 1) was constrained by rutile-ilmenite oxy-barometers for eclogites from the S.W. Tianshan subduction zone (Tao *et al.*, 2017b). In comparison to redox conditions of other subduction belts, the S.W. Tianshan subduction zone has the lowest oxidation condition. If the initial fO_2 of the S.W. Tianshan subduction zone is comparable to a normal altered oceanic crust (between FMQ-1 and FMQ; Foley, 2011), there would be a continuous decrease of fO_2 for the S.W. Tianshan subduction zone during the subduction process to evolve to relatively reduced condition, ranging from FMQ-1.9 to FMQ-2.5. The continuous decrease of fO_2 the subduction zone may result from releasement of oxidized fluid from subducting slabs to the overlying mantle wedge. This is also suggested by previous petrological record by meta-ophiolite from Alps metamorphic belts (Borfecchia *et al.*, 2012; Debret *et al.*, 2014). In other hands, carbonated eclogites have been shown to become more and more reduced as the effect of pressure on the incorporation of Fe^{3+} in garnet (Stagno *et al.* 2015).

The change of redox state of the carbonated slabs during the subduction process should have a big effect on the deep carbon cycle in the subduction zone. The decreased fO_2 of the subduction zone can explain the formation of reduced carbon-bearing phases (e.g. graphite and methane/ethane) from carbonate reduction in the subduction zone (e.g. S.W. Tianshan subduction zone). The decrease of fO_2 by a possible dehydration-redox reaction during the subduction process (Borfecchia *et al.*, 2012; Debret *et al.*, 2014) will transfer carbonate into graphite. The

redox reaction can also change the mobility of carbon-bearing phases from mobile carbonate to immobile graphite in the subduction. This will strongly affect the carbon cycle behavior in the subduction zone. On the other hand, several studies showed the origin of diamonds from deep mantle to be closely linked with the recycled carbonated oceanic crust (Thomson *et al.*, 2014; Kiseeva *et al.*, 2016; Xu *et al.*, 2017; Kiseeva *et al.*, 2018). The generally higher abundances of diamonds are associated with eclogites and with the high proportion of inclusions of eclogitic association in some diamond populations (Cartigny, 2005). Numerous geochemical and isotope studies showed that the deep diamond and its inclusions inherited the characteristic of recycled carbonated slabs (Ickert *et al.*, 2013; Kiseeva *et al.*, 2016). The recycled carbonate would be an important carbon source for deep mantle diamond, too.

5.2 Abiotic hydrocarbons in the subduction zone

Carbonates are the predominant carbon-bearing phases that are commonly present in the subducted slab. They are the potential source of carbon for the abiotic formation of light hydrocarbons and graphite in the subduction zone. We have limited knowledge about the abiotic synthesis of hydrocarbons from carbonates at high pressure and temperature relevant to subduction zones. McCollom (2003) described thermal decomposition of siderite in the presence of water vapor at 300 °C and demonstrated abiotic synthesis of organic compounds dominated by alkylated and hydroxylated aromatic compounds. Milesi *et al.* (2015) investigated the chemical processes governing the carbon speciation associated to hydrothermal decomposition of siderite at 200 - 300 °C and a pressure of 50 MPa, and showed that the gas phase was dominated by CO₂, H₂, and CH₄. These results are complementary to our findings at higher temperatures and

pressures. Our results indicate that the formation of hydrocarbons in the system over wide P-T conditions, although the quantification and kinetics of the reactions require further investigation.

Previous high-pressure experiments on methane formation from the carbonate-H₂O reaction were also performed in a tiny diamond-anvil cell chamber ($< 7 \times 10^{-4} \text{ mm}^3$) at pressures above 5 GPa (Scott *et al.*, 2004; Chen *et al.*, 2008). The experiments at temperatures below 600°C (Chen *et al.*, 2008) were conducted in the resistance-heated diamond-anvil cells, whereas the experiments at higher temperature and pressure were performed using the laser-heating technique (Scott *et al.*, 2004) that have issues such as stable temperature control. Raman spectroscopy was the only diagnostic technique used for the identification of the hydrocarbon compounds. In the experiments of Chen *et al.* (2008), the reduction of calcite (CaCO₃) to form methane was achieved by adding the reducing agents including FeO, SiO, and natural fayalite to water. The characteristic CH stretches were observed by in-situ Raman measurements. Diamond-anvil cell experiments provide excellent in-situ measurements, but they are not ideal for hydrocarbon synthesis because of potential contamination from the diamond anvils (Chou and Anderson, 2009) and the small sample volume. In this study, we used Fe-bearing dolomite (ankerite) and H₂O for the experiments, sealed in a large gold capsule ($\sim 150 \text{ mm}^3$), at least 200 thousand times larger than the diamond-anvil cell chamber, allowing conventional gas content measurements. The reduced carbon species including graphite and hydrocarbons are formed by a disproportionation reaction of Fe²⁺-bearing ankerite and H₂O, accompanied by the formation of Fe³⁺-bearing oxide, magnetite (Fe₃O₄). Because of the large quantity of the gas phases produced in these experiments, we are able to conclusively identify the gas species and quantitatively determine the content of each gas phase by GC measurements, providing details on the production and ratios of the light hydrocarbons including CH₄, C₂H₆, and C₃H₈. In Fig. 8, we

summarize previous experimental studies on the synthesis of abiotic hydrocarbon in a P-T phase diagram, and compare with the experimental conditions in this study. The typical subduction geotherms are also plotted for comparison. Combining our petrological observation and experimental simulation from previous and this study, we propose a possible abiotic formation mechanism of hydrocarbon from the reduction of carbonate at high-pressure and high-temperature conditions, especially in subduction environments with water saturation as the S.W. Tianshan subduction zone (Okamoto and Maruyama, 1999).

6. Conclusions

Both field observations and laboratory experiments have provided conclusive evidence that light hydrocarbons and graphite can form from the reduction of carbonates in the presence of water at high pressure and temperature in subduction environments. The presence of oxidized iron (Fe_3O_4) and reduced carbon species in the system is documented in the field specimen and the recovered experimental charges. This redox reaction could be an important mechanism for generating hydrocarbons in the subduction zone where carbonates and water are abundant. This is further supported by thermodynamic calculations (e.g. French, 1966; Connolly, 1995 and calculations in this study) and Deep Earth Water theoretical models (Sverjensky *et al.*, 2014). We have also demonstrated that heavier hydrocarbons such as ethane and propane, identified by GC measurements, could be synthesized at pressures as low as 1.5 GPa. The significance of finding methane-ethane inclusions in the carbonated eclogite extends to a general abiotic formation of light hydrocarbons associated with Fe-bearing carbonates and reduced fluids in subduction zone settings with low oxygen fugacity. The high-pressure experiments coupled with Raman

spectroscopic and GC measurements open new research opportunities for the detailed study of hydrocarbon formation in the deep earth under well-controlled experimental environments.

ACKNOWLEDGMENTS

This work was supported by the NSF of China (Grants 41520104004; 41502038; 41330210), and by the DREAM project of MOST, China (Grant No. 2016YFC0600408). V.S. acknowledge financial support from the Deep Carbon Observatory. We thank three anonymous reviewers, Associate Editor Dr. Weidong Song for their constructive suggestions to improve this manuscript. We also thank Haifei Zheng and Xiang Wu for their suggestions, and Guiming Shu, Qiang He and Yong Li for their technical assistance. We thank the Smithsonian Institution for providing the natural ankerite sample from Hollopatak, Hungary.

REFERENCES

- Ague, J.J. and Nicolescu, S. (2014) Carbon dioxide released from subduction zones by fluid-mediated reactions. *Nature Geoscience* 7, 355-360.
- Ai, Y.L., Zhang, L.F., Li, X.P. and Qu, J.F. (2006) Geochemical characteristics and tectonic implications of HP-UHP eclogites and blueschists in southwestern Tianshan, China. *Progress in Natural Science* 16, 624-632.
- Alt, J.C., and Teagle, D.A.H. (1999) The uptake of carbon during alteration of ocean crust. *Geochimica et Cosmochimica Acta* 63, 1527-1535.
- Arai, S., Ishimaru, S. and Mizukami, T. (2012) Methane and propane micro-inclusions in olivine in titanoclinohumite-bearing dunites from the Sanbagawa high-P metamorphic belt, Japan: Hydrocarbon activity in a subduction zone and Ti mobility. *Earth and Planetary Science Letters* 353-354, 1-11.
- Atamas, N.A., Yaremko, A.M., Seeger, T., Leipertz, A., Bienko, A., Latajka, Z., Ratajczak, H. and Barnes, A.J. (2004) A study of the Raman spectra of alkanes in the Fermi-resonance region. *Journal of Molecular Structure* 708, 189-195.
- Aulbach, S. and Stagno, V. (2016) Evidence for a reducing Archean ambient mantle and its effects on the carbon cycle. *Geology* 44, 751-754.
- Berner, R.A. (1999) A new look at the long-term carbon cycle. *GSA Today* 9, 1-6.
- Bézos, A. and Humler, E. (2005) The $\text{Fe}^{3+}/\Sigma\text{Fe}$ ratios of MORB glasses and their implications for mantle melting. *Geochimica et Cosmochimica Acta* 69, 711-725.
- Borfecchia, E., Mino, L., Gianolio, D., Groppo, C., Malaspina, N., Martinez-Criado, G., Sans, J.A., Poli, S., Castelli, D. and Lamberti, C. (2012) Iron oxidation state in garnet from a subduction setting: a micro-XANES and electron microprobe (“flank method”) comparative study. *Journal of Analytical Atomic Spectrometry* 27, 1725-1733.

- Brovarone, A.V., Martinez, I., Elmaleh, A., Compagnoni, R., Chaduteau, C., Ferraris, C., and Esteve, I. (2017) Massive production of abiotic methane during subduction evidenced in metamorphosed ophicarbonates from the Italian Alps. *Nature communications* 8, 14134.
- Bryndzia, L.T. and Wood, B.J. (1990) Oxygen thermobarometry of abyssal spinel peridotites: the redox state and C-O-H volatiles composition of the Earth's sub-oceanic upper mantle. *American Journal of Science* 290, 1093-1116.
- Cao, Y., Song, S.G., Niu, Y.L., Jung, H. and Jin, Z.M. (2011) Variation of mineral composition, fabric and oxygen fugacity from massive to foliated eclogites during exhumation of subducted ocean crust in the North Qilian suture zone, NW China. *Journal of Metamorphic Geology* 29, 699-720.
- Cartigny, P. (2005) Stable isotopes and the origin of diamond. *Elements* 1, 79-84.
- Chen, J.Y., Jin, L.J., Dong, J.P., Zheng, H.F. and Liu, G.Y. (2008) Methane formation from CaCO_3 reduction catalyzed by high pressure. *Chinese Chemical Letters* 19, 475-478.
- Chou, I.M. and Anderson, A.J. (2009) Diamond dissolution and the production of methane and other carbon-bearing species in hydrothermal diamond-anvil cells. *Geochimica et Cosmochimica Acta* 73, 6360-6366.
- Christie, D.M., Carmichael, I.S.E. and Langmuir, C.H. (1986) Oxidation states of mid-ocean ridge basalt glasses. *Earth and Planetary Science Letters* 79, 397-411.
- Claypool, G.E., and Kaplan, I.R. (1974) The origin and distribution of methane in marine sediments. *Natural Gases in Marine Sediments*. 99-139.
- Connolly, J.A.D. (1995) Phase diagram methods for graphitic rocks and application to the system C-O-H-FeO-TiO₂-SiO₂. *Contributions to Mineralogy and Petrology* 119, 94-116.
- Dasgupta, R. (2013) Ingassing, storage, and outgassing of terrestrial carbon through geologic time. *Reviews in Mineralogy and Geochemistry* 75, 183-229.
- Debret, B., Andreani, M., Muñoz, M., Bolfan-Casanova, N., Carlut, J., Nicollet, C., Schwartz, S. and Trcera, N. (2014) Evolution of Fe redox state in serpentine during subduction. *Earth and Planetary Science Letters* 400, 206-218.
- Donohue, C.L., and Essene, E.J. (2000) An oxygen barometer with the assemblage garnet-epidote. *Earth and Planetary Science Letters* 18, 459-472.
- Duncan, M.S. and Dasgupta, R. (2017) Rise of Earth's atmospheric oxygen controlled by efficient subduction of organic carbon. *Nature Geoscience* 10, 387-392.
- Etioppe, G., and Schoell, M. (2014) Abiotic Gas: Atypical, But Not Rare. *Elements* 10, 291-296.
- Foley, S.F. (2011) A Reappraisal of Redox Melting in the Earth's Mantle as a Function of Tectonic Setting and Time. *Journal of Petrology* 52, 1363-1391.
- French, B.M. (1966) Some geological implications of equilibrium between graphite and a C-H-O gas phase at high temperature and pressures. *Review of Geophysics* 4, 223-253.
- Frezzotti, M.L., Selverstone, J., Sharp, Z.D. and Compagnoni, R. (2011) Carbonate dissolution during subduction revealed by diamond-bearing rocks from the Alps. *Nature Geoscience* 4, 703-706.
- Froelich, P.N., Klinkhammer, G.P., Berder, M.L., Luedtke, N.A., Heath, G.R., Cullen, D. and Dauphin, P. (1979) Early oxidation of organic matter in pelagic sediments of the eastern equatorial Atlantic: suboxic diagenesis. *Geochimica et Cosmochimica Acta* 43, 1075-1090.
- Frost, B.R. (1979) Metamorphism of iron-formation parageneses in the system Fe-Si-C-O-H. *Economic Geology* 74, 775-785.
- Frost, D.J., and McCammon, C.A. (2008) The redox state of Earth's mantle. *Annual Review of Earth and Planetary Sciences* 36, 389-420.
- Frost, D.J. (2012) The carbon cycle in Earth's interior and the formation of diamonds BGI Annual Report 2012 and lists of publications 3, 19-37.
- Fu, B., Touret, J.L.R., Zheng, Y.-F. and Jahn, B.-m. (2003) Fluid inclusions in granulites, granulitized eclogites and garnet clinopyroxenites from the Dabie-Sulu terranes, eastern China. *Lithos* 70, 293-319.

- Gao, J. and Klemd, R. (2001) Primary fluids entrapped at blueschist to eclogite transition: evidence from the Tianshan meta-subduction complex in northwestern China. *Contributions to Mineralogy and Petrology* 142, 1-14.
- Gao, J., John, T., Klemd, R. and Xiong, X. (2007) Mobilization of Ti–Nb–Ta during subduction: Evidence from rutile-bearing dehydration segregations and veins hosted in eclogite, Tianshan, NW China. *Geochimica et Cosmochimica Acta* 71, 4974-4996.
- Galvez, M.E., Beysac, O., Martinez, I., Benzerara, K., Chaduteau, C., Malvoisin, B. and Malavieille, J. (2013) Graphite formation by carbonate reduction during subduction. *Nature Geoscience* 6, 473-477.
- Giardini, A.A. and Salotti, C.A. (1969) Kinetics and relation in the calcite-hydrogen reaction and relations in the dolomite-hydrogen and siderite-hydrogen system. *American Mineralogist* 54, 1151-1172.
- Gudmundsson, G. and Wood, B.J. (1995) Experimental tests of garnet peridotite oxygen barometry. *Contributions to Mineralogy and Petrology* 119, 56-67.
- Hacker, B.R. (2003) Subduction factory 1. Theoretical mineralogy, densities, seismic wave speeds, and H₂O contents. *Journal of Geophysical Research* 108, 2029.
- Hermes, P., John, T., Bakker, R.J. and Schenk, V. (2012) Evidence for channelized external fluid flow and element transfer in subducting slabs (Raspas Complex, Ecuador). *Chemical Geology* 310-311, 79-96.
- Holland, T.J.B. and Powell, R. (1998) An internally consistent thermodynamic data set for phases of petrological interest. *Journal of Metamorphic Geology* 16, 309-343.
- Holland, T.J.B. and Powell, R. (2011) An improved and extended internally consistent thermodynamic dataset for phases of petrological interest, involving a new equation of state for solids. *Journal of Metamorphic Geology* 29, 333-383.
- Höfer, H.E., Brey, G.P., Schulz-Dobrick, B., and Oberhänsli, R. (1994) The determination of the oxidation state of iron by the electron microprobe. *European Journal of Mineralogy*, 6, 407-418.
- Höfer, H.E., and Brey, G.P. (2007) The iron oxidation state of garnet by electron microprobe: Its determination with the flank method combined with major-element analysis. *American Mineralogist* 92, 873-885.
- Huang, F., Daniel, I., Cardon, H., Montagnac, G., and Sverjensky, D.A. (2017) Immiscible hydrocarbon fluids in the deep carbon cycle. *Nature Communications* 8, 15798.
- Ickert, R.B., Stachel, T., Stern, R.A. and Harris, J.W. (2013) Diamond from recycled crustal carbon documented by coupled $\delta^{18}\text{O} - \delta^{13}\text{C}$ measurements of diamonds and their inclusions. *Earth and Planetary Science Letters* 364, 85-97.
- Isshiki, M., Irifune, T., Hirose, K., Ono, S., Ohishi, Y., Watanuki, T., Nishibori, E., Takata, M. and Sakata, M. (2004) Stability of magnesite and its high-pressure form in the lowermost mantle. *Nature* 427, 60-63.
- Javoy, M., Pineau, F., and Allegre, C.J. (1982) Carbon Geodynamic Cycle. *Nature* 300, 171-173.
- Kelemen, P.B. and Manning, C.E. (2015) Reevaluating carbon fluxes in subduction zones, what goes down, mostly comes up. *Proc. Natl. Acad. Sci. U. S. A.* 112, E3997-4006.
- Kelley, K.A. and Cottrell, E. (2009) Water and the oxidation state of subduction zone magmas. *Science* 325, 605-607.
- Kiseeva, E.S., Wood, B.J., Ghosh, S., and Stachel, T. (2016) The pyroxenite-diamond connection. *Geochemical Perspectives Letters* 2, 1-9.
- Kiseeva, E.S., Vasiukov, D.M., Wood, B.J., McCammon, C., Stachel, T., Bykov, M., Bykova, E., Chumakov, A., Cerantola, V., Harris, J.W., and Dubrovinsky, L. (2018) Oxidized iron in garnets from the mantle transition zone. *Nature Geoscience* 11, 144-147.
- Li, Y. (2016) Immiscible C-H-O fluids formed at subduction zone conditions. *Geochemical Perspectives Letters* 3, 12-21.
- Li, J.L., Klemd, R., Gao, J. and Meyer, M. (2014) Compositional zoning in dolomite from lawsonite-bearing eclogite (SW Tianshan, China): Evidence for prograde metamorphism during subduction of oceanic crust. *American Mineralogist* 99, 206-217.

- Liu, X., Chen, J., Tang, J., He, Q., Li, S., Peng, F., He, D., Zhang, L. and Fei, Y. (2012a) A large volume cubic press with a pressure-generating capability up to about 10 GPa. *High Pressure Research: An International Journal* 32, 239-254.
- Liu, X., Wang, S., He, Q., Chen, J., Wang, H., Li, S., Peng, F., Zhang, L. and Fei, Y. (2012b) Thermal elastic behavior of CaSiO₃-walsstromite: A powder X-ray diffraction study up to 900°C. *American Mineralogist* 97, 262-267.
- Lin, F., Bodnar, R.J. and Becker, S.P. (2007) Experimental determination of the Raman CH₄ symmetric stretching (ν_1) band position from 1–650 bar and 0.3–22°C: Application to fluid inclusion studies. *Geochimica et Cosmochimica Acta* 71, 3746-3756.
- Lollar, B.S., Westgate, T.D., Ward, J.A., Slater, G.F. and Lacrampe-Couloume, G. (2002) Abiogenic formation of alkanes in the Earth's crust as a minor source for global hydrocarbon reservoirs. *Nature* 416, 522-524.
- Lollar, B.S., Lacrampe-Couloume, G., Voglesonger, K., Onstott, T.C., Pratt, L.M. and Slater, G.F. (2008) Isotopic signatures of CH₄ and higher hydrocarbon gases from Precambrian Shield sites: A model for abiogenic polymerization of hydrocarbons. *Geochimica et Cosmochimica Acta* 72, 4778-4795.
- Luth, R.W., Virgo, D., Boyd, F.R. and Wood, B.J. (1990) Ferric iron in mantle-derived garnets: Implications for thermobarometry and for the oxidation state of the mantle. *Contributions to Mineralogy and Petrology* 104, 56-72.
- Luth, R.W. (1993) Diamond, eclogites and the oxidation state of the Earth's mantle. *Science* 261, 66-68.
- Lü, Z., Zhang, L., Du, J. and Bucher, K. (2008) Coesite inclusions in garnet from eclogitic rocks in western Tianshan, northwest China: Convincing proof of UHP metamorphism. *American Mineralogist* 93, 1845-1850.
- Lü, Z., Zhang, L.F., Du, J.X. and Bucher, K. (2009) Petrology of coesite-bearing eclogite from Habutengsu Valley, western Tianshan, NW China and its tectonometamorphic implications. *Journal of Metamorphic Geology* 27, 773-787.
- Lü, Z., Zhang, L., Du, J., Yang, X., Tian, Z. and Xia, B. (2012) Petrology of HP metamorphic veins in coesite-bearing eclogite from western Tianshan, China: Fluid processes and elemental mobility during exhumation in a cold subduction zone. *Lithos* 136-139, 168-186.
- Lü, Z., Bucher, K. and Zhang, L.F. (2013) Omphacite-bearing calcite marble and associated coesite-bearing pelitic schist from the meta-ophiolitic belt of Chinese western Tianshan. *Journal of Asian Earth Sciences* 76, 37-47.
- Malaspina, N., Poli, S. and Fumagalli, P. (2009) The Oxidation State of Metasomatized Mantle Wedge: Insights from C-O-H-bearing Garnet Peridotite. *Journal of Petrology* 50, 1533-1552.
- Malvoisin, B., Chopin, C., Brunet, F. and Galvez, M.E. (2011) Low-temperature wollastonite formed by carbonate reduction: a marker of serpentinite redox conditions. *Journal of Petrology* 53, 159-176.
- Mattinson, C.G., Zhang, R.Y., Tsujimori, T. and Liou, J.G. (2004) Epidote-rich talc-kyanite-phengite eclogites, Sulu terrane, eastern China: P-T- f_{O_2} estimates and the significance of the epidote-talc assemblage in eclogite. *American Mineralogist* 89, 1772–1783.
- Matveev, S., Ballhaus, C., Fricke, K., Truchenbrodt, J. and Ziegenbein, D. (1997) Volatiles in the Earth's mantle: I. Synthesis of CHO fluids at 1273 K and 2.4 GPa. *Geochimica et Cosmochimica Acta* 61, 3081-3088.
- McCammom, C.A., Chaskar, V., and Richards, G.G. (1991) A technique for spatially resolved Mössbauer spectroscopy applied to quenched metallurgical slags. *Measurement Science and Technology*, 2, 657-662.
- McCollom, T.M. (2003) Formation of meteorite hydrocarbons from thermal decomposition of siderite (FeCO₃). *Geochimica et Cosmochimica Acta* 67, 311-317.
- Melton, C.E. and Giardini, A.A. (1974) The composition and significance of gas released from natural diamonds from Africa and Brazil. *American Mineralogist* 59, 775-782.

- Milesi, V., Guyot, F., Brunet, F., Richard, L., Recham, N., Benedetti, M., Dairou, J. and Prinzhofer, A. (2015) Formation of CO₂, H₂ and condensed carbon from siderite dissolution in the 200–300 °C range and at 50MPa. *Geochimica et Cosmochimica Acta* 154, 201-211.
- Okamoto, K. and Maruyama, S. (1999) The high-pressure synthesis of lawsonite in the MORB + H₂O system. *American Mineralogist* 84, 362-373.
- Pan, C., Yu, L., Liu, J. and Fu, J. (2006) Chemical and carbon isotopic fractionations of gaseous hydrocarbons during abiogenic oxidation. *Earth and Planetary Science Letters* 246, 70-89.
- Parkinson, I.J. and Arculus, R.J. (1999) The redox state of subduction zones: insights from arc-peridotites. *Chemical Geology* 160, 409-423.
- Plank, T. (2014) The chemical composition of subducting sediments. *Treatise on Geochemistry* 2nd Edition 4. 607-629.
- Poli, S. (2015) Carbon mobilized at shallow depths in subduction zones by carbonatitic liquids. *Nature Geoscience* 8, 633-636.
- Poli, S., Franzolin, E., Fumagalli, P. and Crottini, A. (2009) The transport of carbon and hydrogen in subducted oceanic crust: An experimental study to 5 GPa. *Earth and Planetary Science Letters* 278, 350-360.
- Scott, H.P., Hemley, R.J., Mao, H.-k., Herschbach, D.R., Fried, L.E., Howard, W.M. and Bastea, S. (2004) Generation of methane in the Earth's mantle: In situ high pressure-temperature measurements of carbonate reduction. *Proc. Natl. Acad. Sci. U. S. A.* 101, 14023-14026.
- Shen, T., Hermann, J., Zhang, L., Lü, Z., Padrón-Navarta, J.A., Xia, B. and Bader, T. (2015) UHP Metamorphism Documented in Ti-chondrodite- and Ti-clinohumite-bearing Serpentinized Ultramafic Rocks from Chinese Southwestern Tianshan. *Journal of Petrology* 56, 1425-1458.
- Shi, G.U., Tropper, P., Cui, W., Tan, J. and Wang, C. (2005) Methane (CH₄)-bearing fluid inclusions in the Myanmar jadeitite. *Geochemical Journal* 39, 503-516.
- Sleep, N.H. and Zahnle, K. (2001) Carbon dioxide cycling and implications for climate on ancient Earth. *Journal of Geophysical Research: Planets* 106, 1373-1399.
- Song, S., Su, L., Niu, Y., Lai, Y. and Zhang, L. (2009) CH₄ inclusions in orogenic harzburgite: Evidence for reduced slab fluids and implication for redox melting in mantle wedge. *Geochimica et Cosmochimica Acta* 73, 1737-1754.
- Stagno, V., Ojwang, D.O., McCammon, C.A. and Frost, D.J. (2013) The oxidation state of the mantle and the extraction of carbon from Earth's interior. *Nature* 493, 84-88.
- Stagno, V., Frost, D.J., McCammon, C.A., Mohseni, H. and Fei, Y. (2015) The oxygen fugacity at which graphite or diamond forms from carbonate-bearing melts in eclogitic rocks. *Contributions to Mineralogy and Petrology* 169. doi.org/10.1007/s00410-015-1111-1.
- Staudigel, H., Hart, S.R., Schmincke, H.U. and Smith, B.M. (1989) Cretaceous ocean crust at DSDP Sites 417 and 418: Carbon uptake from weathering versus loss by magmatic outgassing *Geochimica et Cosmochimica Acta* 53, 3091-3094.
- Sverjensky, D.A., Stagno, V. and Huang, F. (2014) Important role for organic carbon in subduction-zone fluids in the deep carbon cycle. *Nature Geoscience* 7, 909-913.
- Tao, R.B., Fei, Y.W. and Zhang, L.F. (2013) Experimental determination of siderite stability at high pressure. *American Mineralogist* 98, 1565-1572.
- Tao, R., Zhang, L., Fei, Y. and Liu, Q. (2014) The effect of Fe on the stability of dolomite at high pressure: Experimental study and petrological observation in eclogite from southwestern Tianshan, China. *Geochimica et Cosmochimica Acta* 143, 253-267.
- Tao, R., Zhang, L., Liu, X., Bader, T. and Fei, Y. (2017a) Phase relations and formation of K-bearing Al-10 Å phase in the MORB+H₂O system: Implications for H₂O- and K-cycles in subduction zones. *American Mineralogist* 102, 1922-1933.
- Tao, R., Zhang, L., Stagno, V., Chu, X. and Liu, X. (2017b) High-pressure experimental verification of rutile-ilmenite oxybarometer: Implications for the redox state of the subduction zone. *Science China Earth Sciences*.

- Tao, R., Zhang, L., Li, S., Zhu, J. and Ke, S. (2018a) Significant contrast in the Mg-C-O isotopes of carbonate between carbonated eclogite and marble from the S.W. Tianshan UHP subduction zone: Evidence for two sources of recycled carbon. *Chemical Geology* 483, 65-77.
- Tao, R., Fei, Y., Bullock, E.S., Xu, C. and Zhang, L. (2018b) Experimental investigation of Fe³⁺ - rich majoritic garnet and its effect on majorite geobarometer. *Geochimica et Cosmochimica Acta* 225, 1-16.
- Tatsumi, Y. (2005) The subduction factory: How it operates in the evolving Earth. *GSA Today* 15, 4-10.
- Thomson, A.R., Kohn, S.C., Bulanova, G.P., Smith, C.B., Araujo, D., EIMF and Walter, M.J. (2014) Origin of sub- lithospheric diamonds from the Juina- 5 kimberlite (Brazil): constraints from carbon isotopes and inclusion compositions. *Contributions to Mineralogy and Petrology* 168, 1081.
- Tian, Z.L. and Wei, C.J. (2012) Metamorphism of ultrahigh-pressure eclogites from the Kebuerte Valley, South Tianshan, NW China: phase equilibria and P-T path. *Journal of Metamorphic Geology* 31, 281-300.
- White, R.W., Powell, R., and Phillips, G.N., (2003) A mineral equilibria study of the hydrothermal alteration in mafic greenschist facies rocks at Kalgoorlie, Western Australia: *Journal of Metamorphic Geology* 21, 455-68.
- Wood, B.J. and Virgo, D. (1989) Upper mantle oxidation state: Ferric iron contents of lherzolite spinels by ⁵⁷Fe Mössbauer spectroscopy and resultant oxygen fugacities. *Geochimica et Cosmochimica Acta* 53, 1277-1291.
- Woodland, A.B. and O'Neill, H.S.C. (1993) Synthesis and stability of Fe²⁺Fe³⁺₂Si₃O₁₂ garnet and phase relations with Fe₃Al₂Si₃O₁₂ - Fe²⁺Fe³⁺₂Si₃O₁₂ solutions *American Mineralogist* 78, 1002-1005.
- Xiao, Y., Lavis, S., Niu, Y., Pearce, J.A., Li, H., Wang, H. and Davidson, J. (2012) Trace-element transport during subduction-zone ultrahigh-pressure metamorphism: Evidence from western Tianshan, China. *Geological Society of America Bulletin* 124, 1113-1129.
- Xu, C., Kynický, J.i., Tao, R., Liu, X., Zhang, L., Pohanka, M., Song, W. and Fei, Y. (2017) Recovery of an oxidized majorite inclusion from Earth's deep asthenosphere. *Science Advance* 3, 1-7.
- Yang, X., Zhang, L., Tian, Z. and Bader, T. (2013) Petrology and U-Pb zircon dating of coesite-bearing metapelite from the Kebuerte Valley, western Tianshan, China. *Journal of Asian Earth Sciences* 70-71, 295-307.
- Zhang, C. and Duan, Z. (2009) A model for C-O-H fluid in the Earth's mantle. *Geochimica et Cosmochimica Acta* 73, 2089-2102.
- Zhang, L., Ellis, D. and Jiang, W. (2002) Ultrahigh-pressure metamorphism in western Tianshan, China: Part I. Evidence from inclusions of coesite pseudomorphs in garnet and from quartz exsolution lamellae in omphacite in eclogites. *American Mineralogist* 87, 853-860.
- Zhang, L., Ellis, D., Williams, S. and Jiang, W. (2002) Ultra-high-pressure metamorphism in western Tianshan, China Part II. Evidence from magnesite in eclogite. *American Mineralogist* 87, 861-866.
- Zhang, L., Ai, Y. and Song, S. (2007) A brief review of UHP meta-ophiolitic rocks, southwestern Tianshan, Western China. *International Geology Review* 49, 811-823.

FIGURE CAPTIONS

Fig. 1 (a) Geological map of the S.W. Tianshan UHP subduction metamorphic belt, western China, modified after (Lü *et al.*, 2012). The red stars illustrate sample locations in this study. All three samples were collected in the same drainage area of the Habutengsu River.

Fig. 2 BSE image, chemical compositions, phase equilibrium modeling, and oxygen fugacity calculation for carbonated eclogite (K949). (a) BSE image of garnet prophyroblast and equilibrated minerals (e.g. omphacite, paragonite, epidotes). Compositional profile of garnet (number 1 to 7 along red line) and its mineral inclusions (number 6 to 23) are marked on the BSE image (b) Composition profile of garnet prophyroblast: red marks with the line are $\text{Fe}^{3+}/\Sigma\text{Fe}$ ratio profiles of garnet prophyroblast from “Flank method”. (c) P–T pseudosection for K949 calculated in the system NCKMnFMASHO + CO_2 . P-T path recorded by garnet compositional profiles is constrained in the P-T phase diagram as a gray belt. (d) Oxygen fugacity evolution trend of carbonated eclogite (K949) constrained by garnet-omphacite oxybarometer in $\log f_{\text{O}_2}$ vs. T phase diagram at 25 Kbar. The phase boundaries of oxygen fugacity buffers of HM, QFM, DQDG, and IW are thermodynamically calculated using the ThermoCalc program with the improved thermodynamic dataset (Holland and Powell, 2011).

Fig. 3. Photomicrograph, Raman spectrum, BSE image, and oxygen fugacity calculation for carbonated eclogite (H608-23). (a) Photomicrograph of mineral assemblages of H608-23 under crossed polarizing microscopy. (b) Raman spectrum of graphite with dolomite and magnetite in carbonated eclogite (c) BSE image of representative mineral association with graphite associated with fluid-pocket and magnetite (Mgt), surrounded by Fe-dolomite and calcite (Cal), and (d) The calculated P- f_{O_2} phase diagram in the CaO-FeO- CO_2 -O system at 550 °C. In the region A, the ankerite is oxidized into calcite and iron oxide (magnetite or hematite) but without graphite. In the region B, ankerite is coexisting with iron oxide. In the region C, the ankerite will decompose into siderite and aragonite, coexisting with iron oxide. Lowering the oxygen fugacity to the region D, the ankerite reduces to magnetite and graphite. The phase relations were calculated using the ThermoCalc program with the improved internally consistent thermodynamic dataset (Holland and Powell, 2011).

Figure 4. Microphotograph and Raman spectrum of mineral assemblages and fluid inclusions in carbonated eclogite (315-3). (a) Photomicrograph of mineral assemblages in the carbonated eclogites (315-3) under polarizing microscopy. (b) Optical microphotograph of a thin section showing methane/ethane-bearing fluid inclusions in omphacite (Omp) from carbonated eclogite (315-3). (c) Raman spectrum of the gas phase showing the CH stretches from methane and ethane. (d) Raman spectrum of the fluid phase showing OH stretch only.

Figure 5. EDS elemental mapping, BSE images, optical microphotograph, Raman spectrum of run products from high-pressure experiments. (a, b) EDS elemental (carbon) mapping and BSE image indicating formation of abundant of graphite and magnetite in experiment A-C-7 (c)

Optical microphotograph of the run A-C-4 showing assemblage of ankerite (Ank), magnetite (Mgt) and graphite (Gr). Small fluid inclusions in ankerite are visible and large voids filled with graphite are distributed throughout the sample. (d) Raman spectrum of a fluid inclusion in the run A-C-4 showing CH stretches of methane and ethane along with Raman peaks of graphite and ankerite.

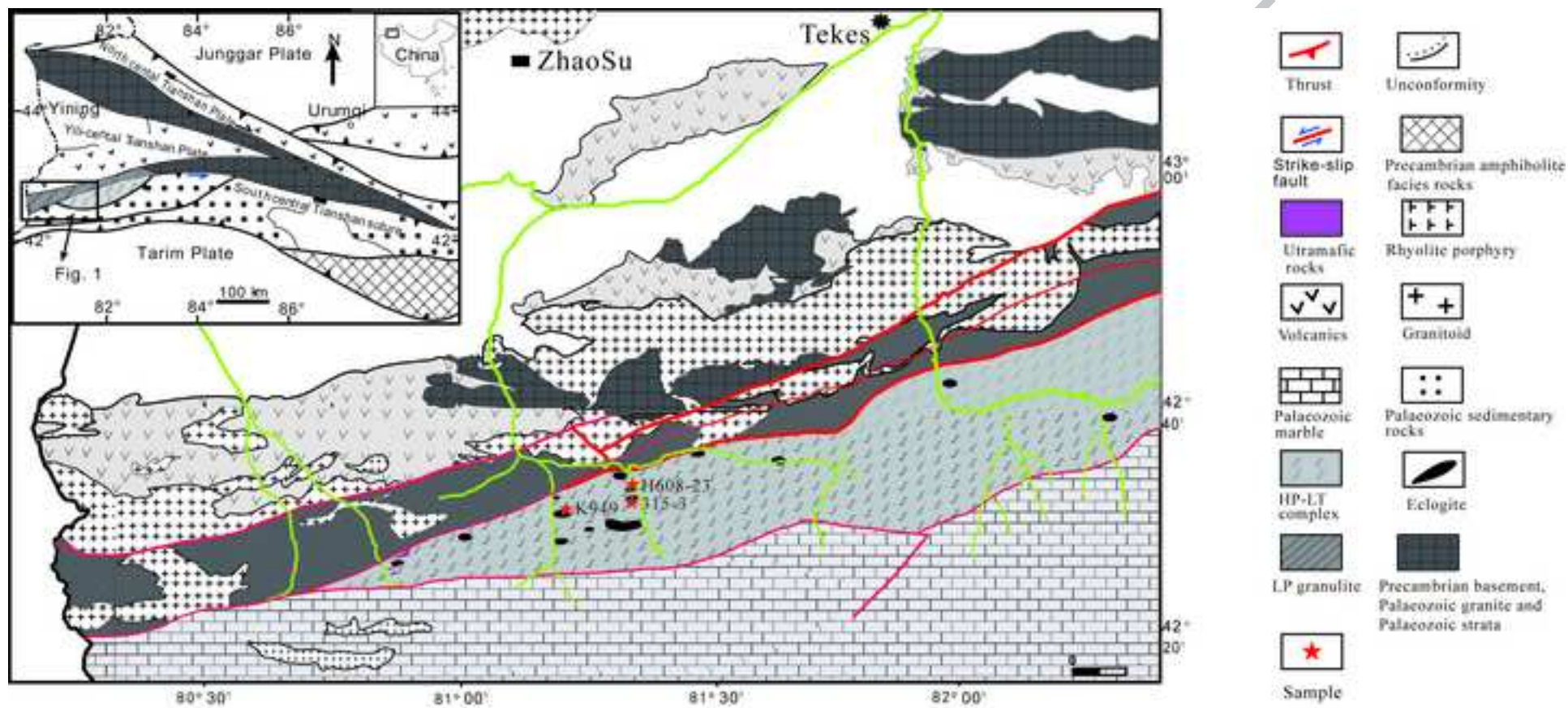
Figure 6. Representative gas chromatograms of the extracted gases from the quenched sample (A-C-7) with background measurements. The gas hydrocarbons including CH₄, C₂H₆, and C₃H₈ were analyzed with the flame ionization detector (FID) and the other gases were analyzed with two thermal conductivity detectors (TCD). Helium (He) and nitrogen (N₂) were used as the carrier gases. The modified gas chromatograph (GC) is equipped with a flame ionization detector (FID) for hydrocarbon analysis and two thermal conductivity detectors (TCD) for analyzing hydrogen, CO₂, and other inorganic gases.

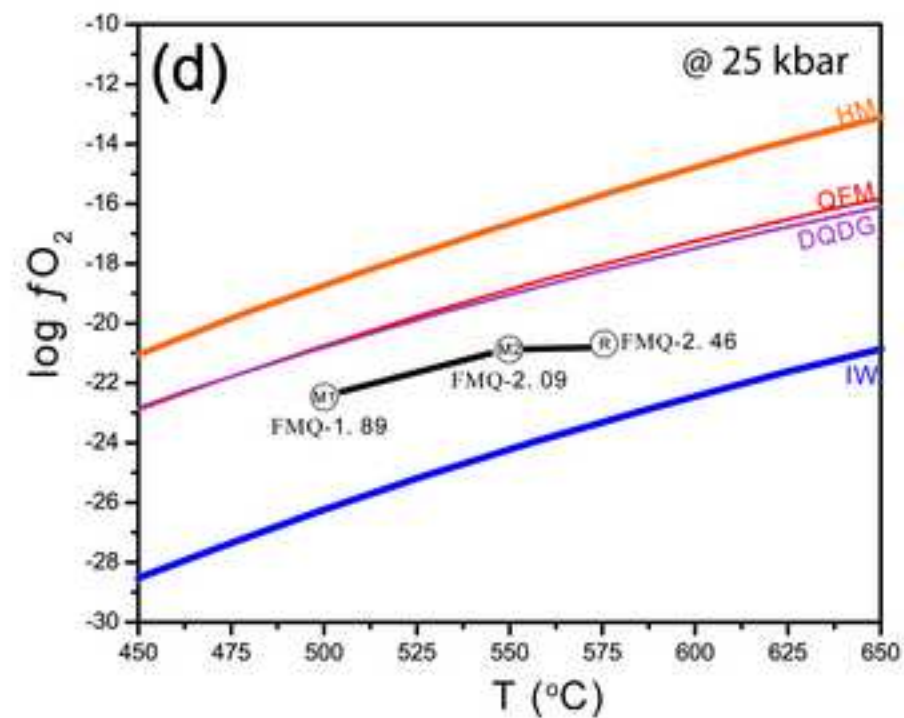
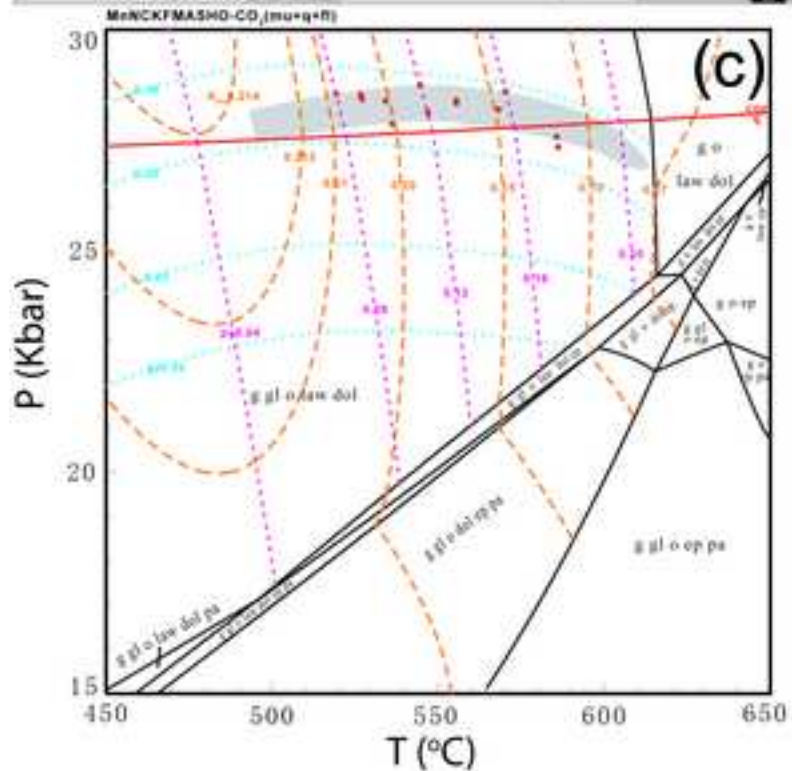
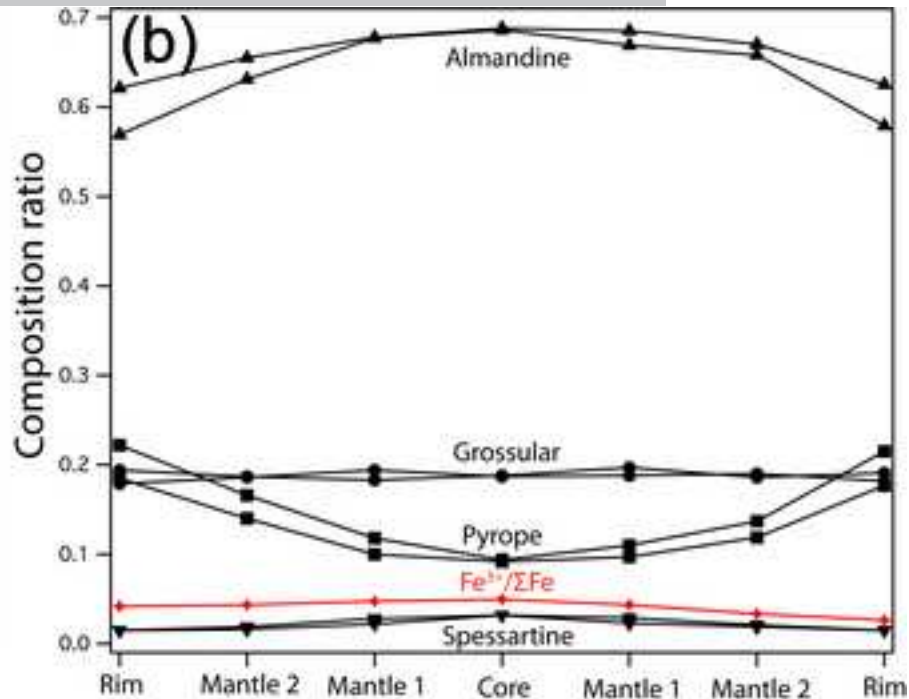
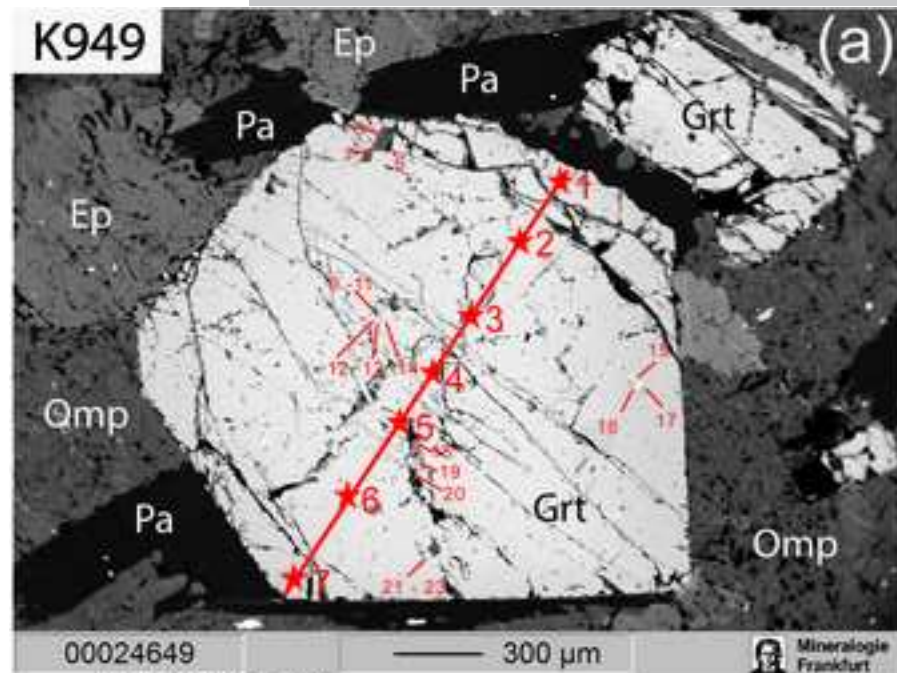
Fig. 7. Comparisons of the estimated oxygen fugacity for different subduction zones. The oxygen fugacity evolution trend of S.W Tianshan subduction zone was constrained by the garnet-omphacite oxybarometer (from M1 to M2, then to R), Fe-dolomite-graphite and magnetite oxybarometer (blue marker), and rutile-ilmenite oxybarometer (orange star). The estimated values of oxygen fugacity for other subduction zones (Eastern Rhodope, Bulgaria; Sulu, China; and North Qilian) were shown for comparison. They have much higher oxygen fugacity than the Southwestern Tianshan subduction zone. The oxygen fugacity of North Qilian is constrained by the garnet-epidote oxybarometer (Mattinson *et al.*, 2004; Cao *et al.*, 2011), whereas the oxygen fugacity of Sulu, China and Eastern Rhodope, Bulgaria are constrained by the garnet peridotite oxybarometer (Malaspina *et al.*, 2009). The C-H₂O oxygen fugacity buffer at 550°C, separating CH₄- and CO₂-rich aqueous fluid (X_O=1/3), was also shown, calculated using the COH model of (Zhang and Duan, 2009). Other oxygen fugacity buffers (CCO, DQDG, HM, IW, QIF and QFM) were calculated using the ThermoCalc program with the improved internally consistent thermodynamic dataset (Holland and Powell, 2011).

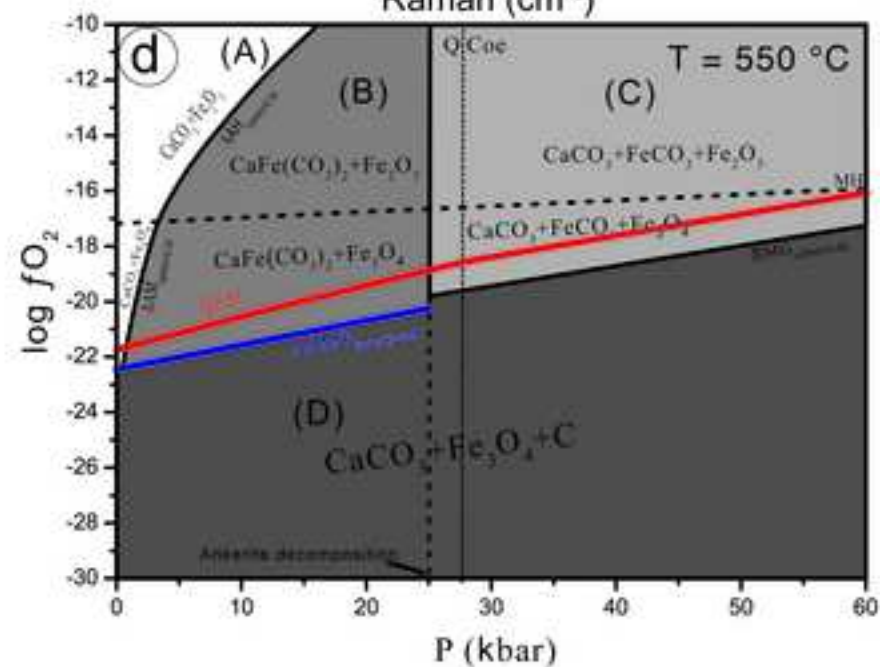
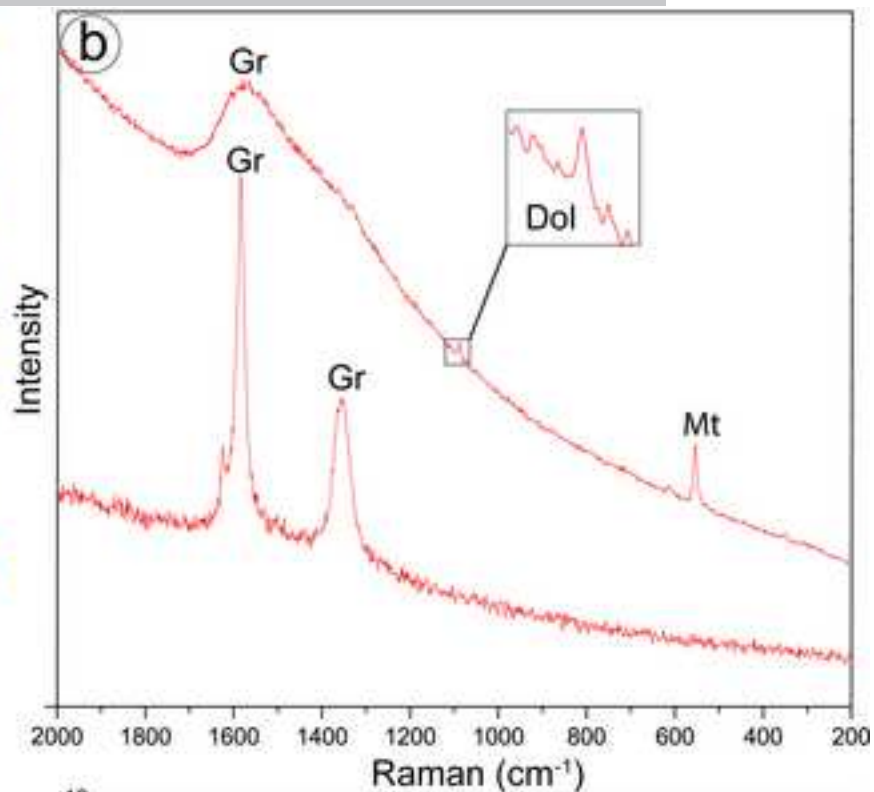
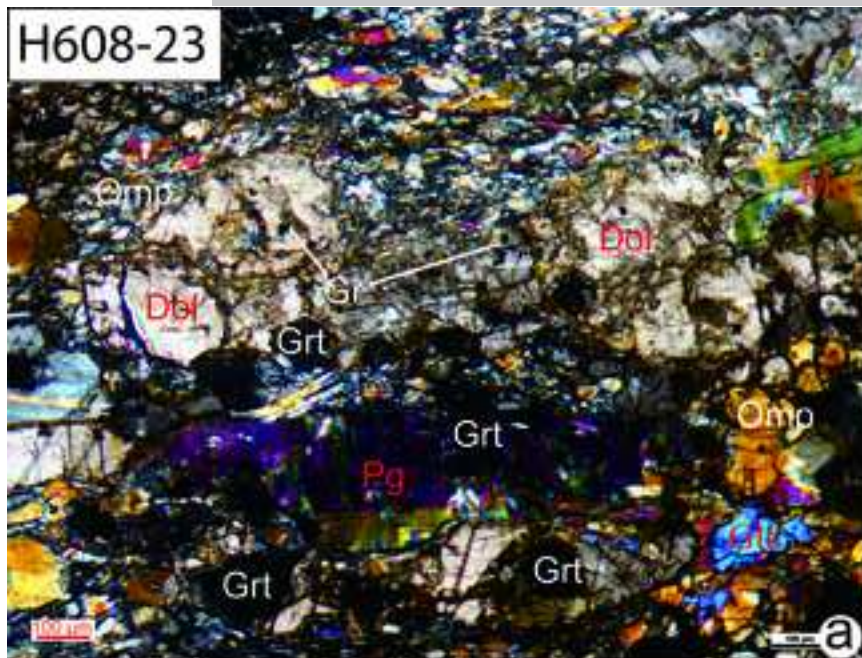
Fig. 8. Summary of P-T conditions of experimental runs in this study in comparison with those from previous studies in similar systems (Scott *et al.*, 2011; McCollom, 2003; Chen *et al.*, 2008; Marocchi *et al.*, 2011; Milesi *et al.*, 2105). Typical subduction and mantle geotherm from Tao *et al.* (2013), and S.W. Tianshan subduction path is also plotted for comparison.

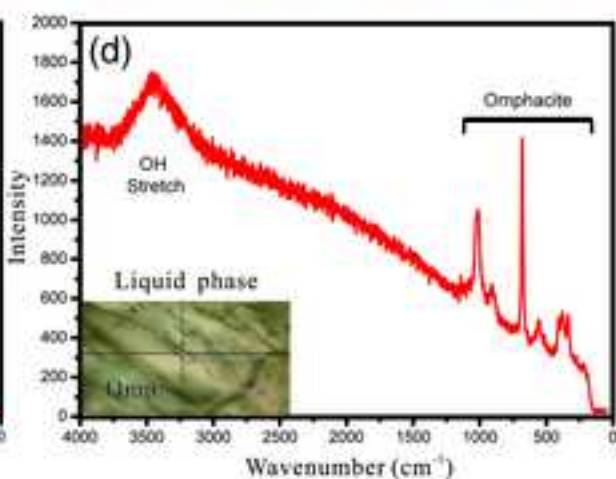
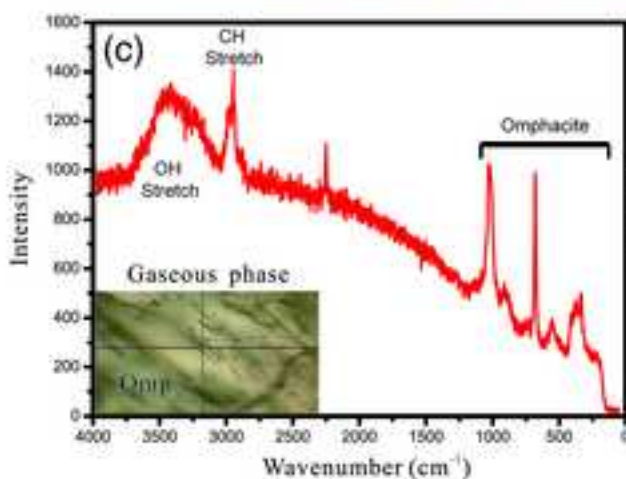
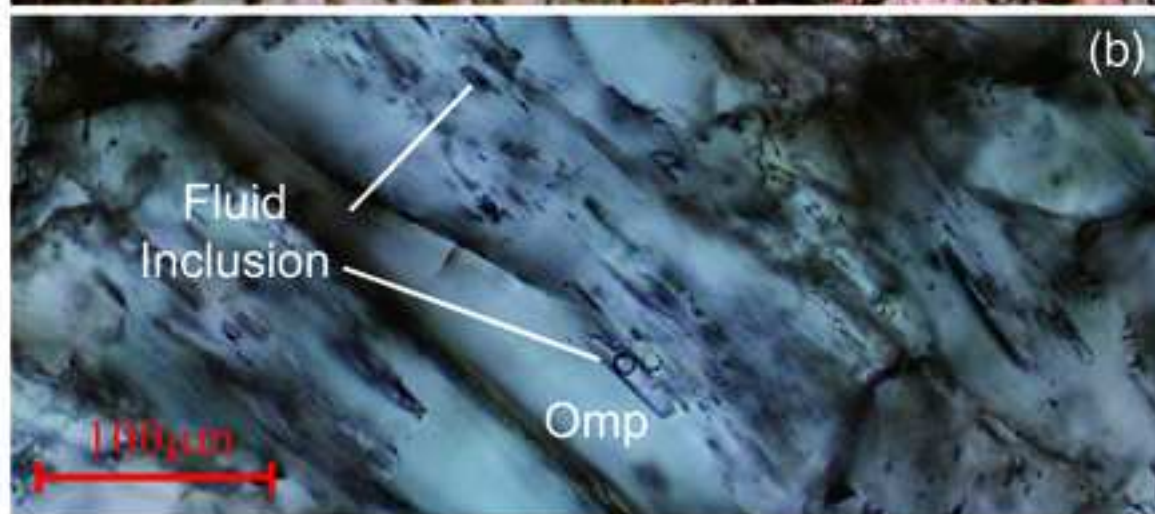
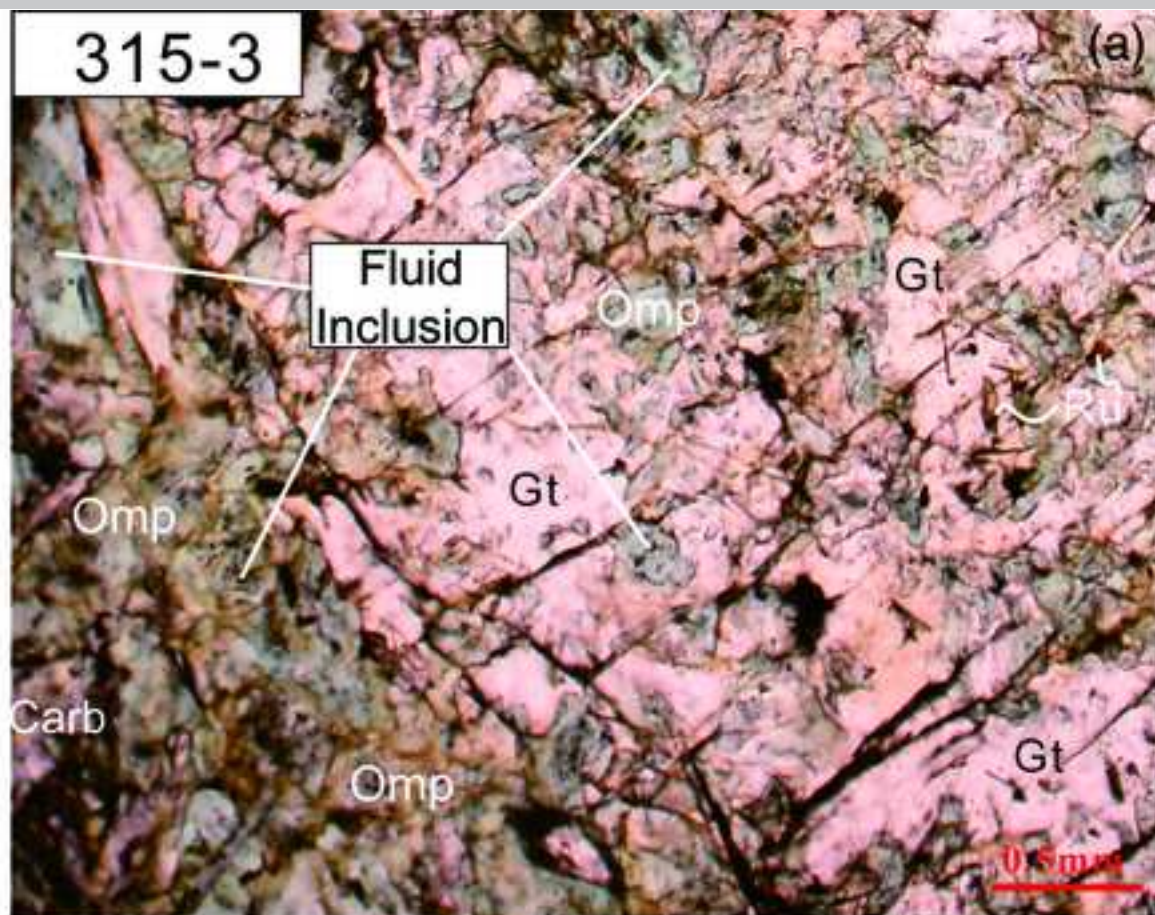
Fig. S1 Chemical composition change of Fe-bearing dolomites in carbonated eclogite (H608-23). Fe contents decrease from light part to dark part on BSE images (Fig. 3c).

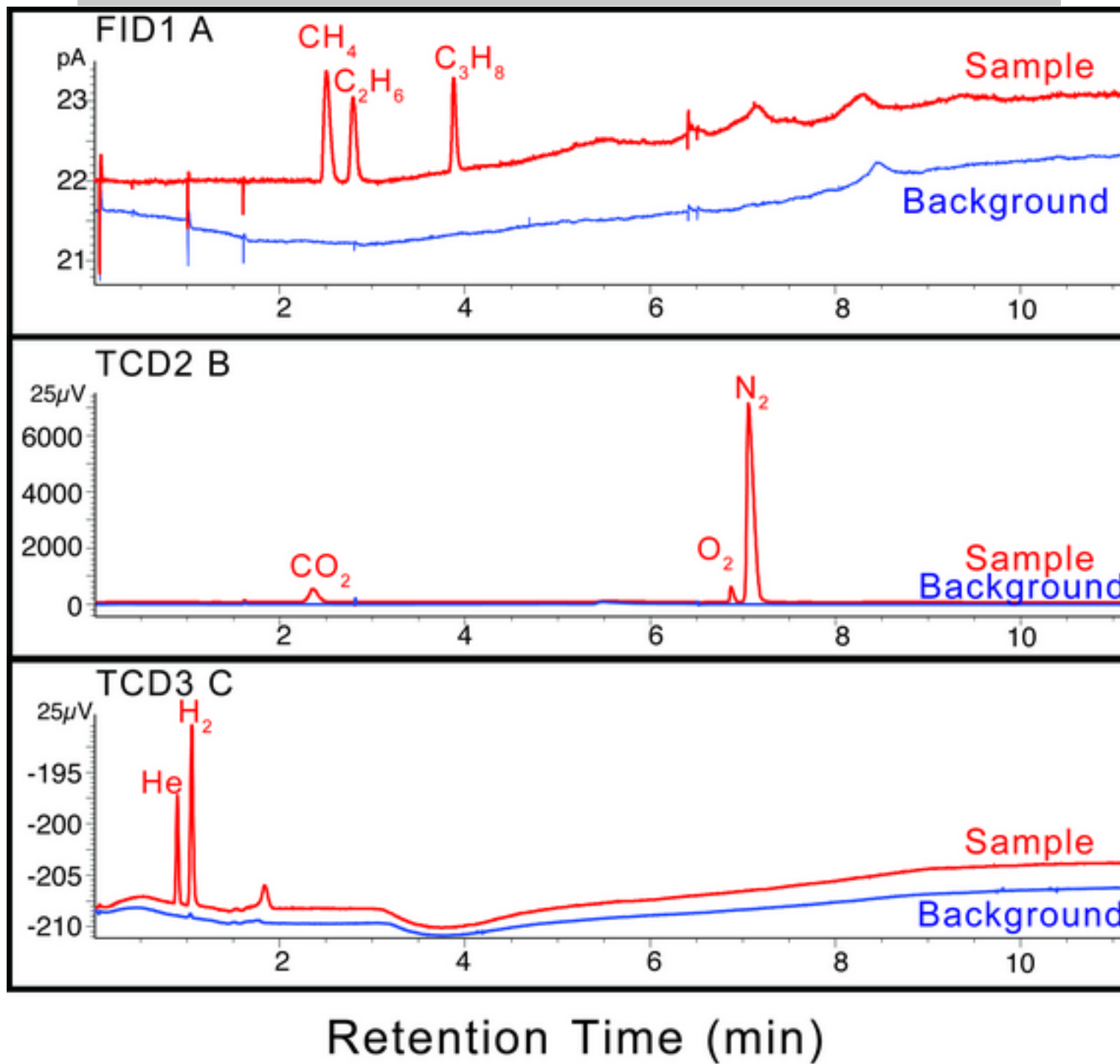
Fig. S2 Chemical composition change of Fe-bearing dolomite from (a) time series experiments, and (b) temperature change experiments. With increasing temperature and longer experiments time, the Fe content of dolomite decreases in the run products.



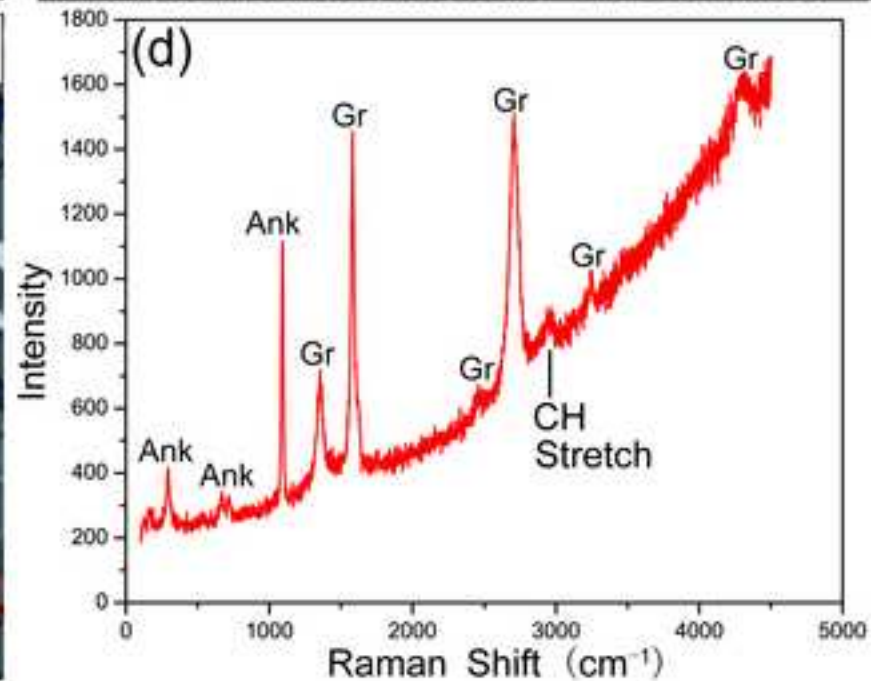
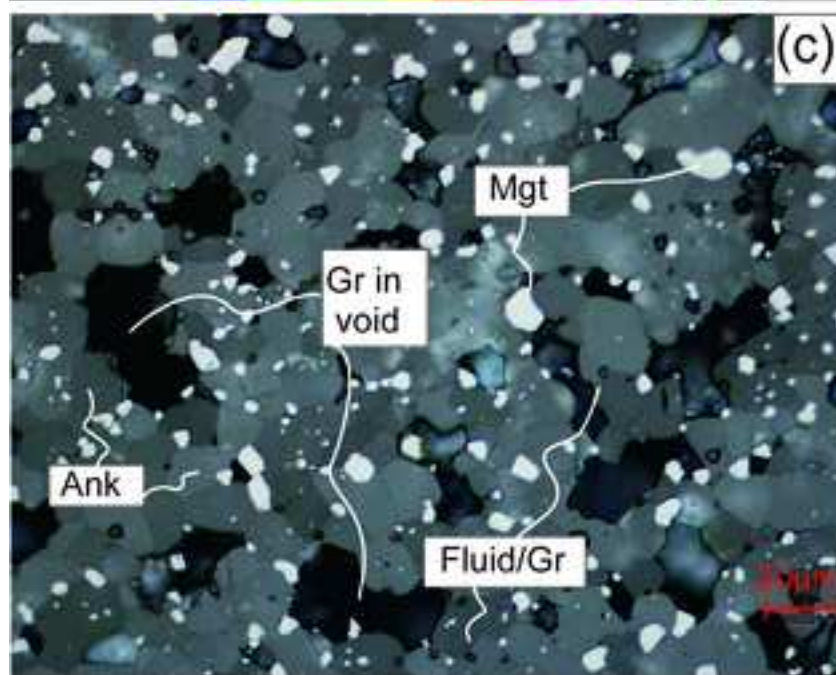
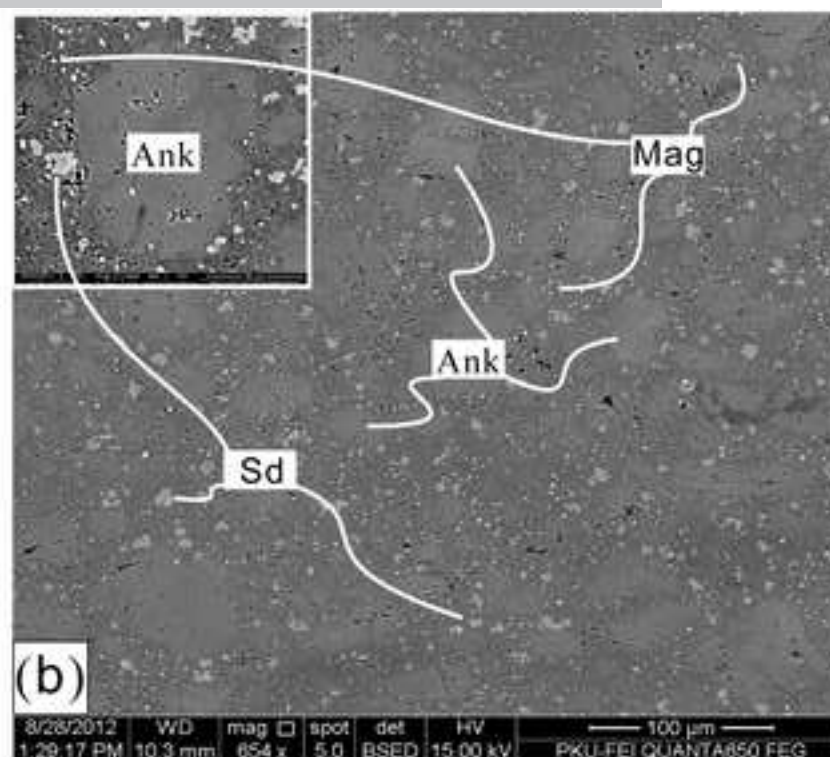
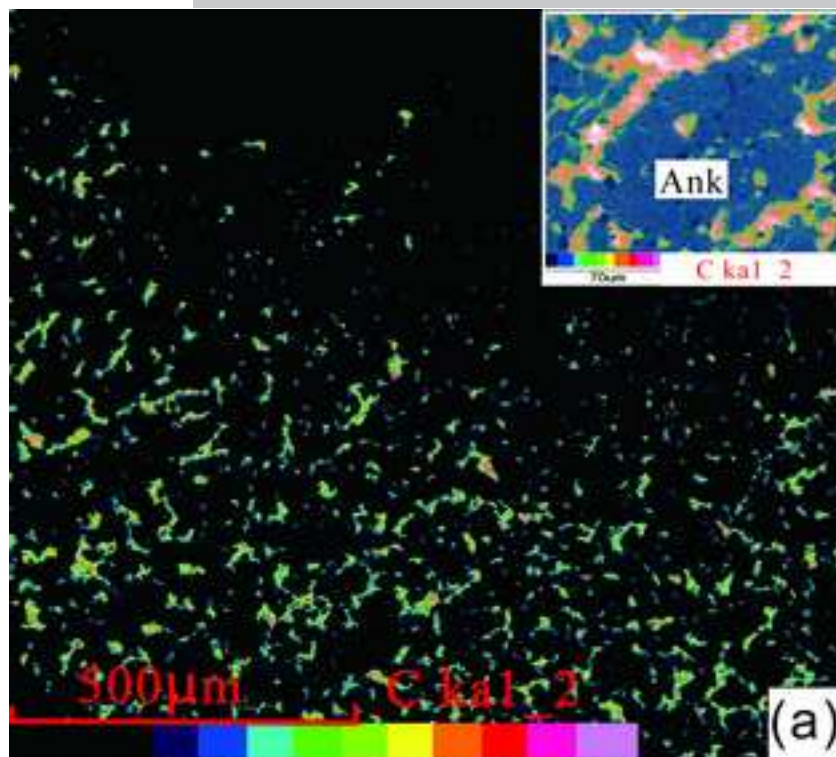


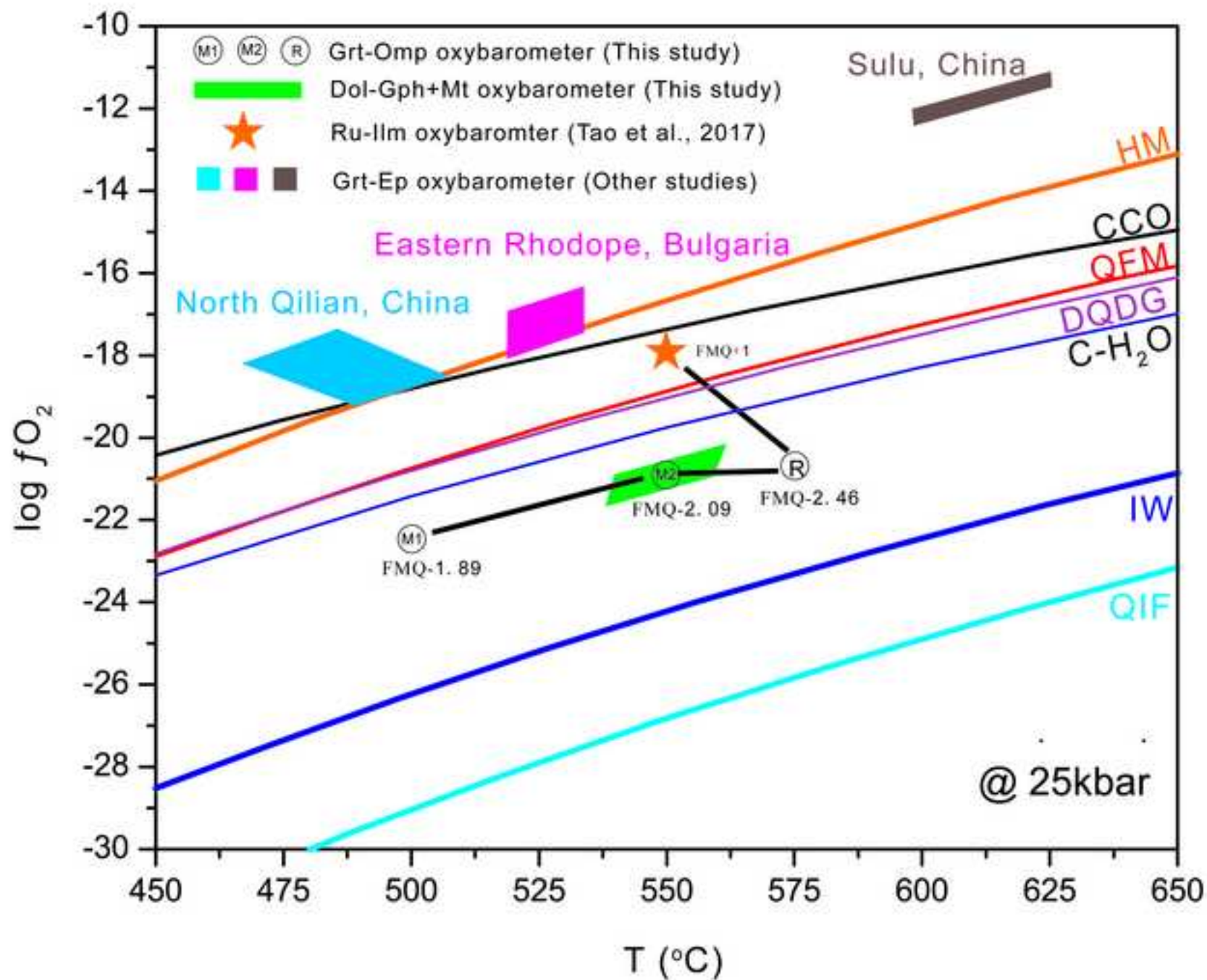






Retention Time (min)





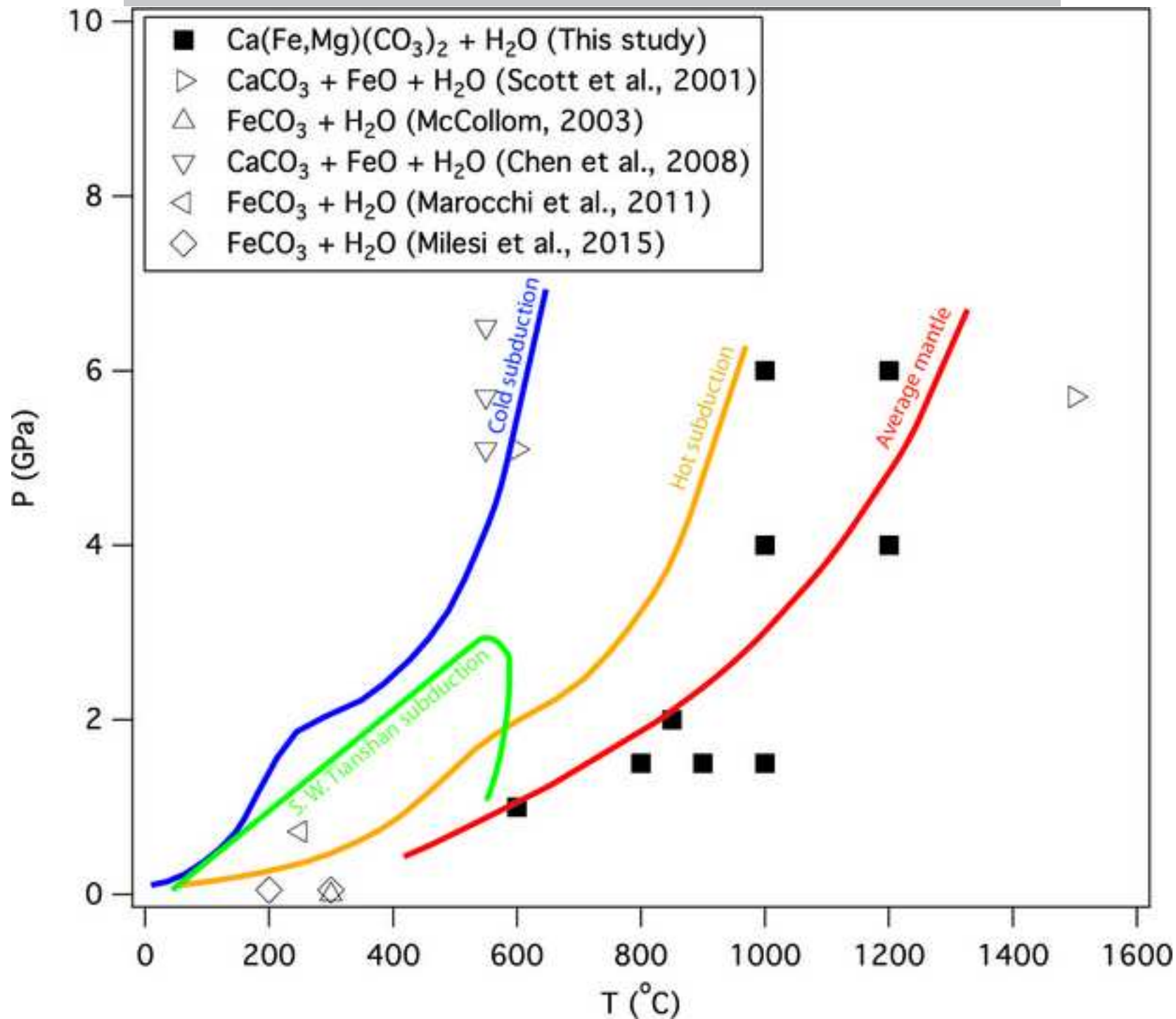


Table 1 Chemical compositions of garnets in carbonated eclogite (K949)

	Sam ple	Gt 1_ 1	Gt 1_ 2	Gt 1_ 3	Gt 1_ 4	Gt 1_ 5	Gt 1_ 6	Gt 1_ 7	Gt 2_ 1	Gt 2_ 2	Gt 2_ 3	Gt 2_ 4	Gt 2_ 5	Gt 2_ 6	Gt 2_ 7
Comp osition	SiO ₂	38. 27	37. 86	37. 63	37. 52	37. 73	37. 80	38. 35	38. 48	38. 23	37. 74	37. 72	37. 83	38. 01	38. 57
	TiO ₂	0.0 4	0.0 6	0.1 0	0.0 6	0.0 8	0.0 7	0.0 4	0.0 2	0.0 4	0.0 6	0.0 8	0.0 8	0.0 6	0.0 3
	Al ₂ O 3	22. 06	21. 76	21. 59	21. 56	21. 63	21. 71	22. 14	22. 24	22. 03	21. 70	21. 58	21. 69	21. 78	22. 13
	Cr ₂ O ₃	0.0 1	0.0 1	0.0 1	0.0 1	0.0 1	0.0 2	0.0 1	0.0 2	0.0 1	0.0 1	0.0 6	0.0 1	0.0 2	0.0 1
	FeO	28. 08	29. 40	30. 18	30. 54	30. 48	29. 96	28. 29	26. 00	28. 62	30. 38	30. 67	29. 98	29. 61	26. 49
	Mn O	0.6 7	0.8 3	1.2 4	1.4 2	1.2 8	0.9 3	0.6 9	0.6 9	0.7 2	0.9 7	1.4 3	1.0 3	0.8 3	0.6 8
	NiO	0.0 0	0.0 0	0.0 0	0.0 0	0.0 0	0.0 0	0.0 0	0.0 0	0.0 0	0.0 0	0.0 0	0.0 0	0.0 0	0.0 0
	Mg O	4.6 9	3.5 3	2.5 0	2.3 0	2.4 3	2.9 7	4.5 0	5.6 9	4.2 3	2.9 7	2.3 5	2.7 7	3.4 6	5.5 3
	CaO	6.3 0	6.5 3	6.7 3	6.4 7	6.5 3	6.6 2	6.4 5	6.9 2	6.6 2	6.4 1	6.5 7	6.8 9	6.5 5	6.8 2
	Na ₂ O	0.0 4	0.0 4	0.0 7	0.0 4	0.0 4	0.0 4	0.0 4	0.0 4	0.0 4	0.0 4	0.0 3	0.0 4	0.0 4	0.0 4
	Tota l	10 0.1 7	10 0.0 2	10 0.0 6	99. 92 0.2	10 0.2 1	10 0.1 3	10 0.5 1	10 0.1 0	10 0.5 4	10 0.2 8	10 0.4 8	10 0.3 1	10 0.3 6	10 0.3 1
cpfu	Si	2.9 9	2.9 9	2.9 9	2.9 9	3.0 0	2.9 9	2.9 9	2.9 9	2.9 9	2.9 9	2.9 9	2.9 9	2.9 9	2.9 9
	Ti	0.0 0	0.0 0	0.0 1	0.0 0	0.0 0	0.0 0	0.0 0	0.0 0	0.0 0	0.0 0	0.0 0	0.0 0	0.0 0	0.0 0
	Al	2.0 3	2.0 3	2.0 2	2.0 3	2.0 3	2.0 3	2.0 4	2.0 3	2.0 3	2.0 3	2.0 2	2.0 2	2.0 2	2.0 2
	Cr	0.0 0	0.0 0	0.0 0	0.0 0	0.0 0	0.0 0	0.0 0	0.0 0	0.0 0	0.0 0	0.0 0	0.0 0	0.0 0	0.0 0
	Fe	1.8 4	1.9 4	2.0 1	2.0 4	2.0 2	1.9 8	1.8 5	1.6 9	1.8 7	2.0 1	2.0 4	1.9 8	1.9 5	1.7 2
	Mn	0.0 4	0.0 6	0.0 8	0.1 0	0.0 9	0.0 6	0.0 5	0.0 5	0.0 5	0.0 6	0.1 0	0.0 7	0.0 6	0.0 4
	Ni	0.0 0	0.0 0	0.0 0	0.0 0	0.0 0	0.0 0	0.0 0	0.0 0	0.0 0	0.0 0	0.0 0	0.0 0	0.0 0	0.0 0
	Mg	0.5 5	0.4 2	0.3 0	0.2 7	0.2 9	0.3 5	0.5 2	0.6 6	0.4 9	0.3 5	0.2 8	0.3 3	0.4 1	0.6 4
	Ca	0.5 3	0.5 5	0.5 7	0.5 5	0.5 6	0.5 6	0.5 4	0.5 8	0.5 5	0.5 4	0.5 6	0.5 8	0.5 5	0.5 7
	Na	0.0 1	0.0 1	0.0 1	0.0 1	0.0 1	0.0 1	0.0 1	0.0 1	0.0 1	0.0 1	0.0 0	0.0 1	0.0 1	0.0 1
Tota l	7.9 9	8.0 0	7.9 9	7.9 9	7.9 9	7.9 9	7.9 9	8.0 0	8.0 0	8.0 0	7.9 9	7.9 9	7.9 9	8.0 0	

Flank Method	Fe ³⁺ /ΣFe	0.0 26	0.0 30	0.0 37	0.0 34	0.0 38	0.0 32	0.0 33	0.0 42	0.0 43	0.0 48	0.0 50	0.0 44	0.0 33	0.0 26
	FeO	27. 35	28. 53	29. 07	29. 51	29. 33	29. 00	27. 35	24. 91	27. 38	28. 93	29. 14	28. 67	28. 62	25. 79
	Fe ₂ O ₃	0.8 2	0.9 7	1.2 3	1.1 5	1.2 8	1.0 6	1.0 5	1.2 1	1.3 8	1.6 0	1.7 0	1.4 5	1.1 0	0.7 8
Note: Chemical compositions from electron probe are in wt%. The cations per formula unit (cpfu) are normalized to 12O.															

ACCEPTED MANUSCRIPT

Table 2. Experimental conditions and products

Run#	Capsule dia. (mm)	P (GPa)	T (°C)	Time (hr)	Run products	Fe [#] of Ank
A-C-0	2.5	1	600	120	Ank, Gr, Mgt, fluid	15
A-C-5	2.5	1.5	900	48	Ank, Gr, Mgt, fluid	16
A-C-2	2.5	1.5	1000	3	Ank, Gr, Mgt, fluid	10
A-C-3	2.5	1.5	1000	8	Ank, Gr, Mgt, fluid	9
A-C-4	2.5	1.5	1000	36	Ank, Gr, Mgt, fluid	8
A-C-1	2.5	2	850	25	Ank, Gr, Mgt, fluid	25
A-C-7	5	1.5	800	72	Ank, Gr, Mgt, Sd, fluid	24
A-C-6	5	4	1200	24	Ank, Gr, Mgt, fluid	23
A-C-8	5	4	1000	24	Ank, Gr, Mgt, fluid	24
A-C-9	5	6	1000	24	Ank, Gr, Mgt, fluid	24
A-C-10	5	6	1200	24	Ank, Gr, Mgt, fluid	24

Two gold capsule diameters were used, OD = 5 mm and OD = 2.5 mm. Mineral abbreviations: Ank, ankerite; Gr, graphite; Mgt, magnetite; and Sd, siderite. Fluid compositions are shown in Table 3. The value of Fe[#] is defined by $Fe^{\#} = [Fe^{2+} / (Ca + Mg + Fe^{2+} + Mn)] \times 100$ and the Fe[#] of the starting material ankerite is 26.

Table 3. The measured gas contents by gas chromatograph (mL)

P(GPa)-T(°C)	1.5-800	6-1000	4-1000	4-1200	6-1200
Gas species	A-C-7 [§]	A-C-9 [§]	A-C-8 [†]	A-C-6 [†]	A-C-10 [†]
CH ₄	0.000692	0.002167	0.000632	0.000417	0.000417
C ₂ H ₆	0.00025	0.000107	0.000039	0.000241	0.000015
C ₂ H ₄	-	-	0.000045	0.000241	0.000028
C ₃ H ₈	0.000146	0.000013	-	0.000153	-
C ₃ H ₆	-	-	0.000024	0.000153	0.000018
I-C ₄ H ₁₀	-	-	-	0.000112	-
N-C ₄ H ₁₀	-	-	-	0.000112	-
C ₄ H ₈	-	-	0.000014	0.000112	-
H ₂	0.005254	0.001198	-	0.000109	0.000443
Total reduced gas	0.006342	0.003485	0.000754	0.00165	0.000921
CO ₂	0.206385	0.00092	0.054095	0.046266	0.046241
Total	0.212727	0.004405	0.054849	0.047916	0.047162
Total reduced gas /Total	0.03	0.79	0.01	0.03	0.02

[§]gas extracted by the needle piecing method; [†]gas extracted by combining the needle piecing and sample crashing method; I-C₄H₁₀, isohexane; N-C₄H₁₀, normal hexane. The uncertainty for the measured gas content is about 0.5% (Pan et al., 2006).

ACCEPTED